

The ASKAP-EMU Early Science Project: 888 MHz Radio Continuum Survey of the Large Magellanic Cloud

Clara M. Pennock,^{1*} Jacco Th. van Loon,¹ Miroslav D. Filipović,² Heinz Andernach,³ Frank Haberl,⁴ Roland Kothes,⁵ Emil Lenc,⁶ Lawrence Rudnick,⁷ Sarah V. White,⁸ Claudia Agliozzo,⁹ Sonia Antón,¹⁰ Ivan Bojčić,² Dominik J. Bomans,^{11,12} Jordan D. Collier,^{2,6,13} Evan J. Crawford,² Andrew M. Hopkins,¹⁴ Kanapathippillai Jeganathan,¹⁵ Patrick J. Kavanagh,¹⁶ Bärbel S. Koribalski,^{2,6} Denis Leahy,¹⁷ Pierre Maggi,¹⁸ Chandreyee Maitra,⁴ Josh Marvil,¹⁹ Michał J. Michałowski,¹²⁰ Ray P. Norris,^{2,6} Joana M. Oliveira,¹ Jeffrey L. Payne,² Hidetoshi Sano,^{21,22,23} Manami Sasaki,²⁴ Lister Staveley-Smith,^{25,26} Eleni Vardoulaki²⁷

¹*Lenard-Jones Laboratories, Keele University, ST5 5BG, UK*

Affiliations are listed at the end of the paper

Accepted XXX. Received YYY; in original form ZZZ

ABSTRACT

We present an analysis of a new 120 deg² radio continuum image of the Large Magellanic Cloud (LMC) at 888 MHz with a bandwidth of 288 MHz and beam size of 13''9 × 12''1, from the Australian Square Kilometre Array Pathfinder (ASKAP) processed as part of the Evolutionary Map of the Universe (EMU) survey. The median Root Mean Squared noise is 58 μJy beam⁻¹. We present a catalogue of 54,612 sources, divided over a GOLD list (30,866 sources) complete down to 0.5 mJy uniformly across the field, a SILVER list (22,080 sources) reaching down to < 0.2 mJy and a BRONZE list (1,666 sources) of visually inspected sources in areas of high noise and/or near bright complex emission. We discuss detections of planetary nebulae and their radio luminosity function, young stellar objects showing a correlation between radio luminosity and gas temperature, novae and X-ray binaries in the LMC, and active stars in the Galactic foreground that may become a significant population below this flux level. We present examples of diffuse emission in the LMC (H II regions, supernova remnants, bubbles) and distant galaxies showcasing spectacular interaction between jets and intracluster medium. Among 14,333 infrared counterparts of the predominantly background radio source population we find that star-forming galaxies become more prominent below 3 mJy compared to active galactic nuclei. We combine the new 888 MHz data with archival Australia Telescope Compact Array data at 1.4 GHz to determine spectral indices; the vast majority display synchrotron emission but flatter spectra occur too. We argue that the most extreme spectral index values are due to variability.

Key words: Magellanic Clouds – surveys – radio continuum: ISM – radio continuum: galaxies – radio continuum: stars – planetary nebulae: general

1 INTRODUCTION

The Large Magellanic Cloud (LMC) is a disrupted barred spiral galaxy interacting with the Milky Way and its nearest neighbour, the Small Magellanic Cloud. The Magellanic Stream is excellent

evidence for this interaction (Mathewson et al. 1974; Murai & Fujimoto 1980). At a distance of ~ 50 kpc (Pietrzyński et al. 2013, 2019; Riess et al. 2019), the gas-rich LMC's close proximity and size allows an exquisitely detailed study of stellar populations and the interstellar medium (ISM) across an entire galaxy, providing a comprehensive picture of star formation, stellar feedback and galaxy structure. It has been a benchmark for astrophysical discoveries,

* E-mail: c.m.pennock@keele.ac.uk

such as the Cepheid period–luminosity relation by Henrietta Leavitt (see [Leavitt 1908](#); [Leavitt & Pickering 1912](#)) and the best-studied supernova, SN 1987A.

At radio frequencies, we typically observe free–free emission from ionized gas in H II regions and planetary nebulae (PNe) and synchrotron emission from supernova remnants (SNRs), as well as from active galactic nuclei (AGN) and star-forming galaxies in the background. The LMC is located away from the Galactic Plane and Galactic Centre, reducing source confusion in the radio band and extinction at UV/optical/near-IR wavelengths. It has been observed multiple times over the years by telescopes such as MOST (Molonglo Observatory Synthesis Telescope; e.g., [Large et al. 1981](#); [Mills 1985](#); [Mauch et al. 2003b](#)), ATCA (Australia Telescope Compact Array; e.g., [Kim et al. 1998](#); [Dickel et al. 2005](#); [Hughes et al. 2007](#); [Murphy et al. 2010](#)), MWA (Murchison Widefield Array; e.g., [For et al. 2018](#)) and Parkes ([Griffith & Wright 1993](#); [Filipovic et al. 1995, 1996, 1998a,b,c,e](#); [Kim et al. 2003](#)). A new generation of radio telescopes, including the Australian Square Kilometre Array Pathfinder (ASKAP; [Johnston et al. 2008](#); [Hotan et al. 2021](#)) can improve upon the resolution, sensitivity and speed of these observations. ASKAP studies of the LMC and Small Magellanic Cloud (SMC, [Joseph et al. 2019](#)) can provide greater details on SNRs, PNe, (super)bubbles and their environments, young stellar objects (YSOs), symbiotic (accreting compact object) binaries, AGN and star-forming galaxies.

The LMC has been the subject of extensive multi-wavelength surveys. These include all-sky surveys such as WISE (Wide-field Infrared Survey Explorer; [Wright et al. 2010](#)) and Gaia ([Gaia Collaboration et al. 2018a](#)), as well as Magellanic Cloud specific surveys such as SAGE (Surveying the Agents of a Galaxy’s Evolution; [Meixner et al. 2006](#)), HERITAGE (HERschel Inventory of the Agents of Galaxy Evolution; [Meixner et al. 2010](#)), VMC (VISTA Magellanic Cloud; [Cioni et al. 2011, 2017](#)), SMASH (Survey of the Magellanic Stellar History; [Nidever et al. 2017](#)) and sections of the LMC surveyed by XMM–Newton ([Haberl 2014](#)).

At radio frequencies AGN and galaxies dominate the source counts. Hence, multi-wavelength surveys from X-ray to far-infrared (far-IR) combined with the new EMU ASKAP data provide a prime opportunity to study a large population of high redshift AGN in the direction of the LMC. These AGN, once found, while interesting in their own right, can be used as a reference frame for proper-motion studies of the LMC (e.g., [Kallivayalil et al. 2006](#); [Costa et al. 2009](#); [Pedreros 2011](#); [van der Marel & Kallivayalil 2014](#); [Vieira et al. 2014](#); [Schmidt et al. 2020](#)) and to probe the interstellar medium through the LMC (e.g., [Haberl et al. 2001](#)). The ASKAP’s unprecedented sensitivity and resolution allows us to detect and resolve stellar and diffuse sources within the LMC and foreground allowing more systematic radio investigations of populations of such objects ahead of the next generation Square Kilometre Array.

The LMC was selected as a prime target for the Early Science Project (ESP) as part of the ASKAP ([Johnston et al. 2008](#); [Hotan et al. 2021](#)) commissioning and early science verification. ASKAP is a radio interferometer that allows us to survey the LMC with a sensitivity down to the μJy range and a large field of view of 30 deg^2 ([Murphy et al. 2013](#); [Leahy et al. 2019](#)). Here we present a new source catalogue from the ASKAP ESP for radio point sources observed towards the LMC, obtained from a mosaic of images taken at 888 MHz ($\lambda = 34 \text{ cm}$).

This paper is laid out as follows: Section 2 describes the data used to create the source lists. In section 3 we describe the creation of the source catalogue and compare our work to previous catalogues of point sources towards the LMC and SMC. In section 4 we discuss

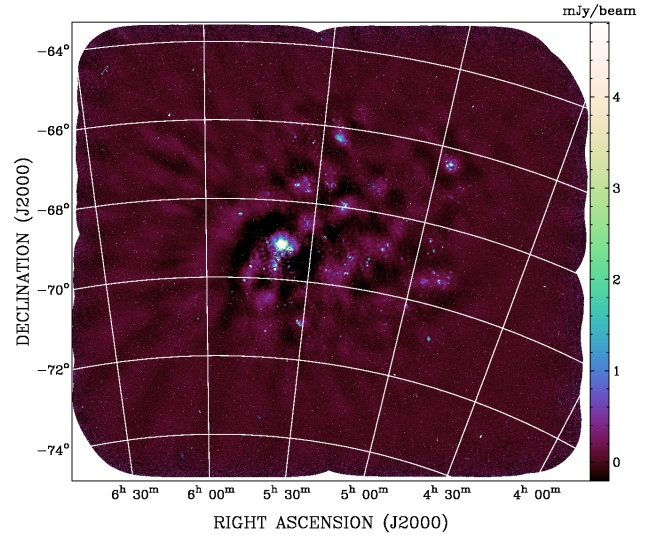


Figure 1. ASKAP ESP image of the LMC at 888 MHz. The beam size is $13''.9 \times 12''.1$

the Magellanic and Galactic foreground sources. Lastly, in section 5 we discuss the sources seen beyond the LMC and in section 6 we determine and discuss the spectral indices of sources in the new catalogue. The source catalogue and 888 MHz image are made available publicly.

2 DATA, OBSERVING AND PROCESSING

Here we present an analysis of the observation of the LMC at 888 MHz with a bandwidth of 288 MHz taken on 2019 April 20 using ASKAP’s full array of 36 antennas (scheduling block 8532). The LMC was observed as part of the ASKAP commissioning and early science (ACES, project code AS033) verification ([DeBoer et al. 2009](#); [Hotan et al. 2014](#); [McConnell et al. 2016](#)) in order to investigate issues that were found in higher-frequency higher-spectral-resolution Galactic-ASKAP (GASKAP; [Dickey et al. 2013](#)) survey observations, as well as to test the rapid processing with ASKAPsoft ([Whiting 2020](#)). The observations cover a total field of view of 120 deg^2 , with a total exposure time of $\sim 12\text{h}40\text{m}$. It is compiled by four pointings ($\sim 3\text{h}10\text{m}$ each) with three interleaves¹ each to result in more uniform depth across the field – effectively 12 pointings. The three interleaves overlap by $\sim 0.5 \text{ deg}$ to improve the uniformity of sensitivity across the field. The ASKAP ESP image of the LMC can be seen in Figure 1. Figures 2 and 3 show close ups of well known LMC regions 30 Doradus (the Tarantula Nebula) and LHA 120-N 119, an H II region near the kinematic centre of the LMC. The largest angular scales that can be recovered in this survey are 25–50 arcmin ([McConnell et al. 2020](#)). The LMC exhibits structure on scales larger than can be recovered by the shortest baselines available with ASKAP (22 m). The missing short-spacing data results in negative bowls around some regions, for example, this is particularly evident around the extended bright structure in 30 Doradus.

Although the image noise levels are near to expected values in most areas, a common feature of early ASKAP data has been the

¹ interleaves are overlapping pointings where the telescope slews between them at a more rapid cadence.

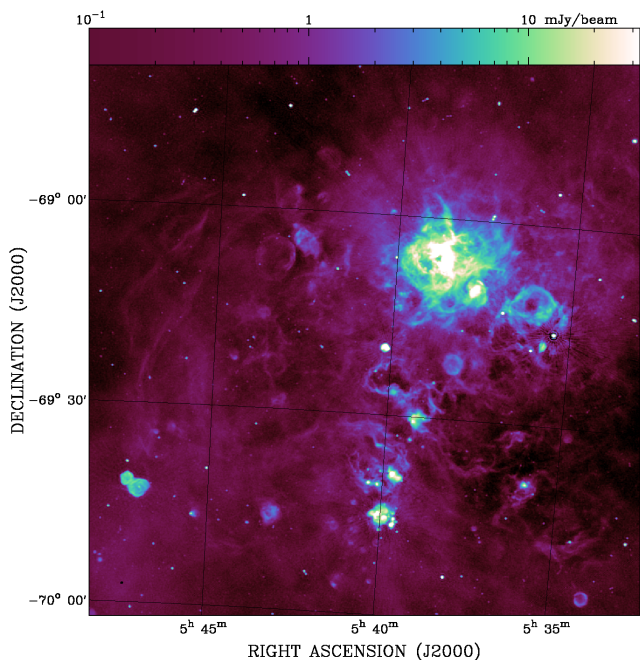


Figure 2. Region around 30 Doradus from the ASKAP ESP image of the LMC.

presence of some low-level artefacts (at ~ 1 per cent peak brightness) very close to bright sources (a few hundred mJy and above). These artefacts generally appear as radial stripes and rapidly fade away from the source.

Data processing was performed using ASKAPsoft (Whiting 2020) by the ASKAP operations team and the resulting images are available on the CSIRO ASKAP Science Data Archive². Bandpass calibration was done using observations of PKS B1934–638, which establishes the flux scale and frequency-dependent complex gains for each of ASKAP’s 36 beams. The bandpass-calibrated measurement set for each beam is imaged independently using a phase-only self-calibration approach. The multi-scale, multi-frequency CLEAN algorithm was used to deconvolve the array response, with two Taylor terms representing spectral behaviour. Images for all beams were combined into a single field using a linear mosaic, correcting for the primary beam response.

The absolute flux density calibration uncertainty is tied to PKS B1934–638 (ATNF Technical Document Ser. 39.3/040³), which differs by no more than 1–2 per cent compared to the Baars scale (Baars et al. 1977). Additional uncertainties are introduced by point spread function (PSF) variation in a mosaic, generally ~ 1 –2 per cent for long-track observations such as this one. In later observations this is alleviated by convolving each beam image to the smallest possible common PSF (McConnell et al. 2020). Uncertainties are also introduced by the assumption that all beams have a consistent Gaussian primary beam-shape. In reality holography has shown that they are somewhat non-Gaussian (particularly edge and corner beams of the phased-array instantaneous field) differing from a Gaussian shape by up to 8 per cent (McConnell et al. 2020). Therefore, the overall absolute flux density calibration uncertainty is 8 per cent.

² <https://research.csiro.au/casda/>

³ <https://www.atnf.csiro.au/observers/memos/d96783.1.pdf>

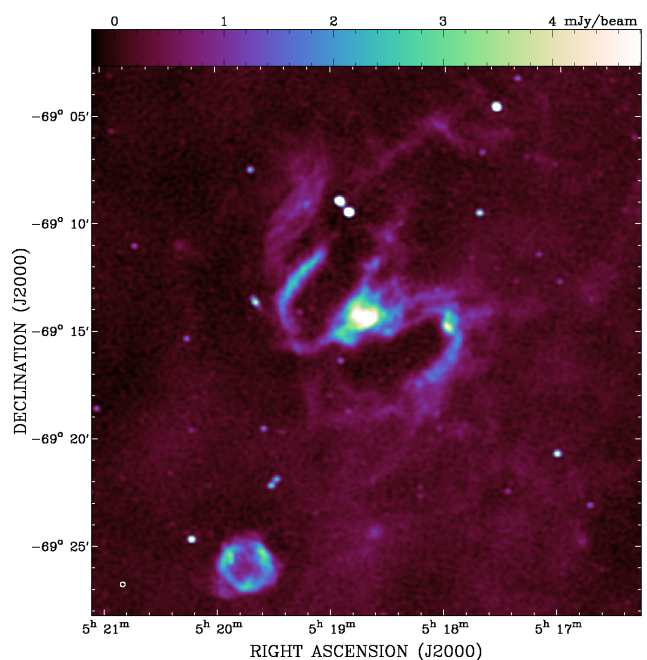


Figure 3. LHA 120-N 119 from the ASKAP ESP image of the LMC. N 119 is an H II region close to the kinematic centre of the LMC, and has a pronounced spiral shape that is reminiscent of a barred spiral galaxy.

3 ASKAP ESP LMC SOURCE LIST

3.1 Source detection

We created the 888 MHz LMC ASKAP source catalog using the AEGEAN source finder algorithm (Hancock et al. 2012; Hancock et al. 2018). Variable noise is present across the image, from the combination of the multiple beams and artefacts from bright sources. To ensure accurate source thresholds the variable noise must be parameterised before source finding. The BANE (Background and Noise Estimation) routine in the AegeanTools software was used, with default parameters, to create root mean squared noise (RMS) and background level maps⁴. The maps were then used, alongside the LMC image, with AEGEAN, using default parameters to create initial source lists. A cursory visual inspection of the sources was carried out to verify detections from the initial source list.

To ascertain the best AEGEAN parameters, the algorithm was used on subsamples of the image with different values of SEEDCLIP (the number of σ above the local RMS for sources to be deemed detected) to find the best SEEDCLIP value that obtains the least false positive detections without sacrificing too many true positive detections. To quantify the false detection rate we can assume that the noise in the image follows a symmetric, Gaussian distribution. This symmetry means that the negative image (inverted) has the same noise properties as the non-inverted image, meaning large noise troughs in the original image are now detected as sources. Hence, the number of detected sources should be approximately equal to the number arising from the false positive noise spikes in the true image. From this we can constrain the “real” detections in an image by investigating how the false detections vary with SEEDCLIP and

⁴ It does this via a sliding boxcar approach where it calculates the background and noise properties of all pixels within a box centred on a given grid point, the resulting maps having the same pixel scale as the input images.

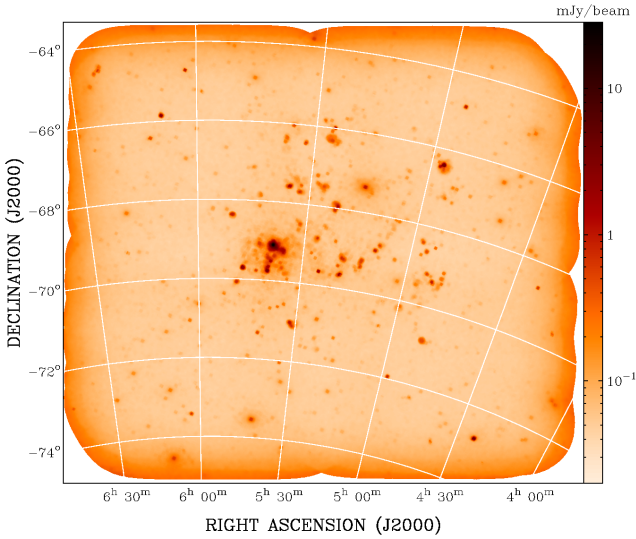


Figure 4. RMS map of the 888 MHz ASKAP observations, produced by BANE with the default parameters. The image is of the same pixel scale as in Figure 1. Higher RMS levels are found at the edge of the field (due to fewer beams present and because of the primary beam shape of which the sensitivity falls off) and around the brighter sources.

then pick out the optimum value that successfully extracts sources with minimal contamination from noise (Hale et al. 2019). The percentage of real detections can therefore be calculated using

$$\%RealDetections = 100 \times \frac{N_+ - N_-}{N_+} \quad (1)$$

where N_+ and N_- are the total number of sources detected with AEGEAN on the original and inverted images, respectively. Testing proved that for a large variety of regions, containing from compact to large extended sources, the default value of 5σ was appropriate.

3.2 Source lists

In total, we found 54,612 sources in the ASKAP 888 MHz image. We separated this source list into a GOLD (30,866), SILVER (22,080) and BRONZE (1,666) source list. Some sample records of the GOLD source list can be found in Table 1. The PSF was generated during image restoration, which means that the semi-major axis ($13''9$), semi-minor axis ($12''1$) and position angle (-84.4°) of the PSF are constant for all sources. The sizes of the sources were determined during source finding. All sources have a designated 'Island' number, and if multiple sources have the same 'Island' number then they are considered components of the island and will have different 'Source' numbers. These components of the islands can be spread across the different source lists. The isolated (one component in an island) sources make up ~ 90 per cent of the entire catalogue. We note that isolated sources have more reliable flux density errors than sources that are components of islands, which tend to have unreasonably small flux density errors calculated by AEGEAN.

To remove multiple detections of large/bright extended sources, a threshold of the local RMS was used. This is because in the area of these large sources the value of local RMS is higher than elsewhere. A cut of $RMS < 0.12$ mJy was used and a cursory visual inspection was undertaken of the sources removed (and not removed) to verify the effectiveness of this cut. This cut also had the effect of removing sources close to/surrounded by bright extended

sources, as well as the sources along the outermost edges of the image due to the poorer sensitivity in this part of the image.

The GOLD standard source list was selected to be a spatially uniform distribution of sources, so that the fainter sources, that are not uniform in spatial distribution, are separated into a SILVER source list (see Figure 5 (left & centre)). For a source to be moved to the SILVER list an integrated flux density of at most 0.5 mJy was required. This value was chosen because this is where the flux density distribution of the ASKAP radio sources turns over, see Figure 6. The BRONZE source list was created, which consists of the sources that were removed with the local RMS cutoff but judged subsequently to be true sources. Each source was individually visually inspected using SAOImageDS9 (Joye & Mandel 2003), where a source was kept if it was clearly visible above the background noise and was point-like or slightly resolved. This reclaimed some of the sources near the edge of the image where the high noise removed them from the SILVER and GOLD lists, as well as the sources that were near bright extended emissions, including well-known bright sources such as the supernova SN 1987A. The sources that were not recovered are those located in complex regions or blended with other sources that would require higher angular resolution to disentangle. The flux densities of a few sources in noisy or confused regions may be unreliable. Therefore, it is advised that for these sources the user inspects the image and ascertain whether to trust the given flux density values. Of the 4,072 sources originally removed, 1,666 were placed in the BRONZE source list, the density map of which is presented in Figure 5 (right).

3.3 Comparison with previous radio catalogues

The ASKAP ESP source lists were compared with various radio continuum catalogues that cover the LMC. The number counts for our survey were compared with those from the previous ASKAP ESP catalogue of the SMC (Joseph et al. 2019), for which the full ASKAP array was not available. See Table 2 for a comparison of previous radio surveys of the LMC.

3.3.1 SUMSS 843 MHz

The MOST telescope was used to carry out the Sydney University Molonglo Sky Survey (SUMSS; Mauch et al. 2003b,a) at 843 MHz with a beam size of $45'' \times 45''$ to create a catalogue that covers the whole sky South of $DEC = -30$ deg, including the LMC. The positions in the catalogue are accurate to within 1–2 arcsec for the brighter sources (> 20 mJy beam $^{-1}$) and always better than 10 arcsec. This catalogue therefore makes for a suitable comparison for the new 888 MHz ASKAP catalogue.

The new ASKAP 888 MHz source lists (GOLD and SILVER, 53,547 sources) were cross-matched with the SUMSS 843 MHz catalogue (3,829 sources), with a search radius of 10 arcsec, yielding 3,211 matches. The flux densities are compared in Figure 7; the dashed blue line indicates the one-to-one relation and the red line indicates the line of best fit. The sources that show higher than expected flux density from ASKAP compared to SUMSS were found to be near bright point sources with nearby artefacts which, when coinciding with a fainter source, increases their total flux density. The sources that show lower than expected flux density from ASKAP compared to SUMSS were found to be extended sources, that were seen as one source in SUMSS but multiple components in ASKAP, hence the lower flux density. The correlation between the calculated integrated flux densities of ASKAP 888 MHz and

Table 1. Example of the catalogue created from the LMC ASKAP ESP image. In the second part of the "EMU ID" the sources are labelled either as "ES" or "EC", where "E" stands for early science data, "S" stands for an isolated source and "C" stands for a component of a source. The σ indicates the source-finding fitting error. "Peak" indicates the peak flux density per beam and error. "Integrated" indicates the integrated flux density, which is not fit directly but is calculated from a , b and peak flux and the synthesised beam size. The a is the fitted semi-major axis, b is the fitted semi-minor axis and PA is the fitted position angle. "Island" is the number of the island from which the source was fit and the "Source" is the number within that island, starting from zero for components of a source (EC) and always zero for isolated sources (ES). "Background" is the flux density per beam measured from the background map created with BANE at the source position. "Local RMS" is the flux density per beam measured from the rms map created with BANE at the source position. "Residual Flux" mean and standard deviation are the mean and standard deviation of the residual flux remaining in the island after fitted Gaussian is subtracted. Flags are 0 for a good fit, 2 indicates an error occurred during the fitting process (e.g., the fit did not converge), 4 indicates a component was forced to have the shape of the local point spread function.

Source List	EMU ID	RA (J2000) <i>h m s</i>	Dec (J2000) <i>° ' "</i>	— peak —		— integrated —	
				F (mJy beam ⁻¹)	σ (mJy beam ⁻¹)	F (mJy)	σ (mJy)
GOLD	EMU ES J063120.8–741322	06:31:20.8	–74:13:23	6.20	0.11	7.60	0.14
GOLD	EMU ES J063111.1–741304	06:31:11.3	–74:13:04	1.65	0.08	4.56	0.25
GOLD	EMU ES J062722.6–742301	06:27:22.6	–74:23:01	1.46	0.11	1.67	0.14
GOLD	EMU ES J062920.3–741744	06:29:20.4	–74:17:45	0.74	0.11	0.75	0.12
GOLD	EMU ES J063221.4–740905	06:32:21.4	–74:09:06	9.74	0.11	11.40	0.14
...							

Table 1 – continued

— a —		— b —		— PA —		Island	Source	Background (mJy beam ⁻¹)	Local RMS (mJy beam ⁻¹)	Residual Flux		flags
($''$)	σ ($''$)	($''$)	σ ($''$)	$^\circ$	σ ($^\circ$)					mean (mJy)	σ (mJy)	
15.49	0.07	13.51	0.06	–87.07	0.10	113	0	0.009	0.114	–0.038	0.146	0
27.27	0.39	17.28	0.23	–87.08	0.08	115	0	0.007	0.111	0.007	0.189	0
16.18	0.32	12.05	0.22	–86.66	0.19	117	0	0.015	0.118	–0.013	0.075	0
14.12	0.65	12.21	0.56	–78.88	0.82	118	0	0.007	0.113	–0.006	0.025	0
15.10	0.04	13.24	0.04	–84.38	0.07	119	0	0.004	0.116	–0.010	0.100	0
...												

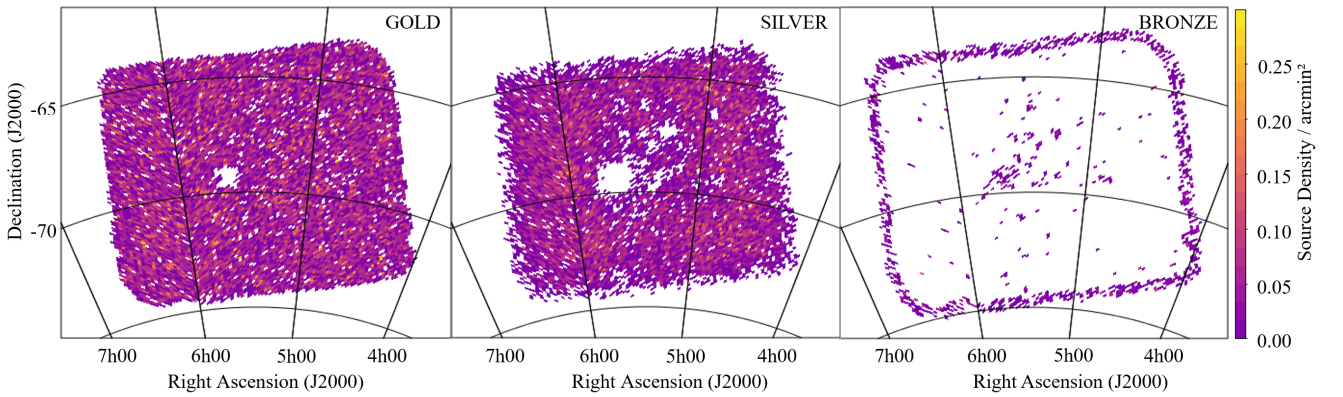


Figure 5. Density plots of the GOLD (left), SILVER (centre) and BRONZE source lists (right). This shows that the GOLD source list is uniform across the LMC field, except in the area of 30 Doradus, which is seen as a blank space. The SILVER source list is not as uniform and showcases gaps where the brighter Magellanic sources are present. The BRONZE source list covers the edges of the LMC field and the areas of the brightest sources, where the local RMS is greatest.

SUMSS 843 MHz source lists is described by the Pearson Correlation Coefficient, $r = 0.967 \pm 0.004$, showing a strong positive correlation and that LMC ASKAP is well flux calibrated.

In Figure 7 the red line is slightly "above" the density ridge of the source distribution, so could be interpreted by the expectation that the small frequency difference from 843 to 888 MHz causes on average a lower flux density at 888 MHz. For $\alpha = -0.7$ (typical of synchrotron emission) this would be $(888\text{MHz}/843\text{MHz})^{-0.7} = 0.96$, whereas the true mode of the integrated flux density ratio is (0.946 ± 0.005) , which is only a little smaller than expected.

We compare the positional differences (ΔRA and ΔDEC) be-

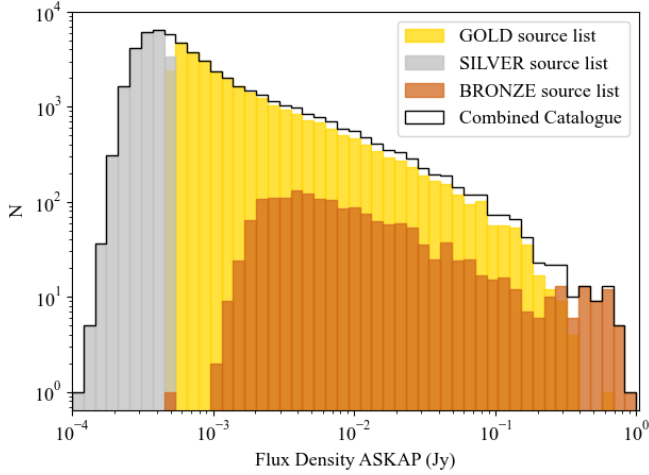
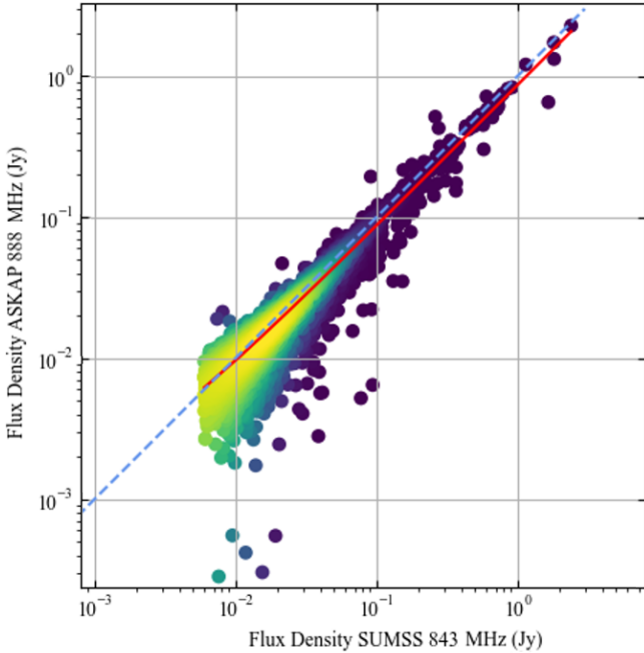
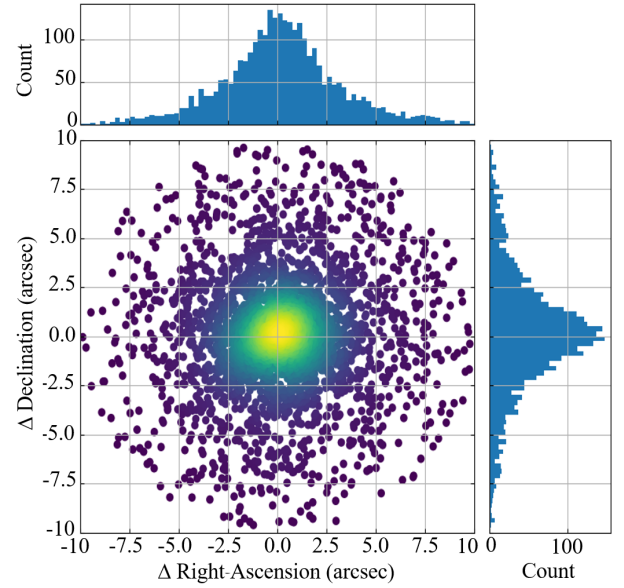
tween our new ASKAP catalogue and the previous SUMSS catalogue at 843 MHz in Figure 8. This figure shows that the positional offsets are well centred, with the mean offsets calculated to be $(0.189 \pm 0.054)''$ and $(0.088 \pm 0.054)''$ for RA and DEC, respectively. Overall, the ASKAP LMC astrometry is well-calibrated.

3.3.2 ASKAP SMC ESP

Two radio continuum images from the ASKAP survey in the direction of the SMC were taken as part of the EMU Early Science Project (ESP) survey of the Magellanic Clouds (Joseph et al. 2019).

Table 2. Table comparing existing radio surveys of the LMC with the survey presented here.

Survey	Telescope	Frequency GHz	RMS mJy beam ⁻¹	Beam Size "	Bandwidth MHz	Source Count	Reference
EMU ESP	ASKAP	0.888	0.0577	13.9 × 12.1	256	53547	This Work
ASKAP-Beta	ASKAP	0.843	0.71	61 × 53	1	1995	Filipović (2021)
1.384 GHz ATCA	ATCA	1.384	0.5	40	128	6623	Hughes et al. (2007)
4.8 / 8.64 GHz ATCA	ATCA	4.8 / 8.64	0.28 / 0.5	33 / 20	128	801 / 419	Dickel et al. (2005)
SUMSS	MOST	0.843	~ 1	43	3	3829	Mauch et al. (2003b)
PMN Survey	Parkes	4.85	~ 4.2	126	600	410	Griffith & Wright (1993)
843 MHz MOST	MOST	0.843	0.3 – 0.4	43	3	2162	Mills (1985)

**Figure 6.** Histogram of integrated flux density at 888 MHz illustrating the GOLD, SILVER, and BRONZE populations.**Figure 7.** Comparison between the integrated flux densities calculated for the ASKAP 888 MHz image, and those from calibrated archival data of SUMSS MOST 843 MHz data. The blue dashed line indicates the one-to-one relation and the red line is the line of best fit. This shows a tight correlation. The outliers in the lower part of the figure are the single SUMSS sources that were resolved by ASKAP into multiple components.**Figure 8.** Figure of positional difference (MOST – ASKAP) of the 2,949 radio sources from the ASKAP (888 MHz) catalogue and the SUMSS (843 MHz) catalogue.

The 888 MHz observation of the LMC covers four times the area of the ASKAP SMC ESP observations. The two source lists that were produced from these images by Joseph et al. (2019) contain radio continuum sources observed at 960 MHz (4489 sources) and 1320 MHz (5954 sources) with a bandwidth of 192 MHz and beam sizes of $30'' \times 30''$ and $16.''3 \times 15.''1$, respectively. The median RMS noise values were $186 \mu\text{Jy beam}^{-1}$ (960 MHz) and $165 \mu\text{Jy beam}^{-1}$ (1320 MHz). The observations of the SMC were made with only 33 per cent and 44 per cent (for 960 MHz and 1320 MHz respectively) of the full ASKAP antenna configuration and 66 per cent of the final bandwidth that was available in the final array, with which the LMC was observed.

Figure 9 shows the number of sources as a function of flux density for ASKAP LMC (888 MHz), ASKAP SMC (960 MHz and 1320 MHz) and SUMSS LMC (843 MHz). As expected, the number of sources is lower and the detection limit is higher in the ASKAP SMC catalogue compared to the ASKAP LMC catalogue. This is due to the smaller survey area, the differences in sensitivity for each image and the observing frequency.

The comparison of the SMC (960 MHz) sources with the LMC sources (888 MHz) where the SMC is scaled up to the same area size as the LMC (see Figure 10), shows increased sensitivity with the array fully operational and that within the flux limits of the SMC

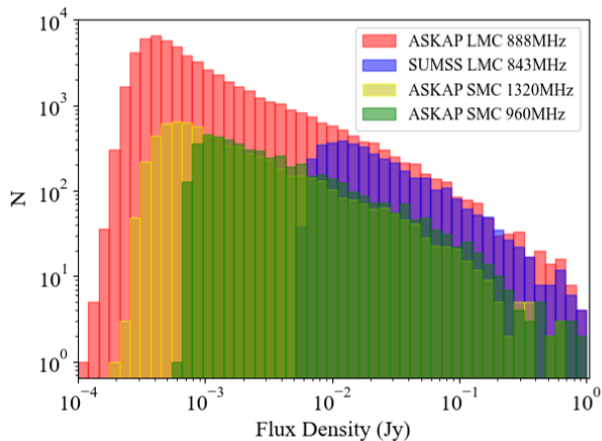


Figure 9. Integrated flux density histograms of ASKAP LMC (888 MHz), ASKAP SMC (960 MHz & 1320 MHz) and SUMSS LMC (843 MHz). The new ASKAP LMC image shows a marked improvement in sensitivity for a radio survey of the LMC and compared to the ASKAP SMC survey.

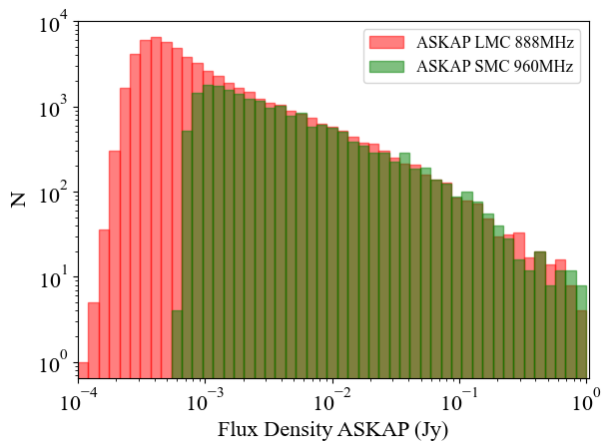


Figure 10. Comparison between the integrated flux densities calculated for the ASKAP images, of the LMC and SMC at 888 MHz and 960 MHz, respectively. The SMC numbers have been scaled to the same of the LMC image for better comparison.

both LMC and SMC ASKAP fields show a similar source density. In contrast to the SMC observation, the LMC observation goes deep enough to surpass the upturn in the luminosity function and probes the radio-faint population (for more details see section 5). Overall, this shows the improvement of using the fully operational ASKAP array. Lastly, the LMC and SMC (the foreground sources) do not fill the area (at least not at high source density) of the ASKAP images, which means that the Clouds do not contribute a significant fraction to the predominantly extragalactic source density.

4 MAGELLANIC AND GALACTIC SOURCES

We discuss a few types of Magellanic and Galactic sources here. These sources were found by cross-matching with various catalogues using TOPCAT⁵ (Taylor 2005) with an initial search radius of 10 arcsec⁶, after which visual inspection was used to determine whether they are true counterparts. All quoted flux densities from

⁵ <http://www.star.bris.ac.uk/~mbt/topcat/>

⁶ to allow for inaccuracies in both the ASKAP and literature positions.

the comparison catalogues are integrated flux densities unless stated otherwise.

4.1 Planetary Nebulae and other emission-line objects

Leverenz et al. (2017) (see also Filipović et al. 2009) presented radio detections of 28 PNe in the LMC, but these were mostly detected at 4.8 GHz (26) with only 14 detected at 1.4 GHz as the radio emission is dominated by free-free emission. Simbad lists 1,334 objects within the ASKAP footprint that have at one time been classed as a PN or candidate PN. Of these, 114 have counterparts in our ASKAP catalogue within 10 arcsec. An example of this list of objects is shown in Table 3 (the full table is available online as a supplementary material). Note that in some cases we believe the (candidate) PN is not the radio counterpart, especially for positional differences of > 6 arcsec.

However, only 43 of these have a primary Simbad class of PN (or candidate PN) and two of these turn out not to be PNe (extended radio emission) and another four have highly uncertain radio detections (a noise spike in one case, two cases of blends, and HD 269404 described below), leaving 37 good radio detections of likely PNe. Another 23 are classed as candidate post-asymptotic giant branch (post-AGB) objects, of which one has an uncertain radio detection (and is discarded) and another one is classed as a carbon-rich Wolf-Rayet star.

This radio sample of 114 radio sources also includes 31 emission-line stars and (three) YSOs, of which two are discarded because of their large positional differences > 9 arcsec, and another 19 compact H II regions or other extended and/or bright radio sources that are likely also H II regions. It is unclear whether there are any post-AGB objects among the emission-line stars.

Among the more interesting sources are HD 269404 = IRAS 05216–6753 ($F_{888} = 3.77 \pm 0.11$ mJy) – still listed in Simbad as a PN but probably a young, massive dust-enshrouded star (van Loon et al. 2001, 2010); and LMC SySt-23 ($F_{888} = 0.37 \pm 0.05$ mJy) – a confirmed D-type symbiotic binary (van Aarle et al. 2011; Akras et al. 2019). One of the most interesting true PNe is SMP LMC 83 ($F_{888} = 1.36 \pm 0.07$ mJy) – with a nitrogen-rich Wolf-Rayet type central star ([WN4.5:]) betraying a massive AGB star progenitor commensurate with it being the radio loudest PN in this sample.

The cumulative histogram of integrated flux densities of the PNe (Figure 11) rises rapidly towards the faint end. The turnover of the distribution at $F_{888} \sim 0.5$ mJy can be attributed to incompleteness; a similar turnover can be seen in the integrated flux density distribution of candidate post-AGB objects. However, the candidate post-AGB distribution is less steep at the faint side of the turnover, compared to the PNe. This may reflect the evolutionary timescale, with a low-mass post-AGB system evolving more slowly and therefore not ionizing its circumstellar envelope as efficiently. Possibly, the brighter sources descend from massive AGB progenitors and are surrounded by a larger ionized envelope and/or a higher electron density compared to lower-mass systems. The distinction between post-AGB and PN is not sharply defined, though, and some of the post-AGB objects may well be considered to be PNe.

The emission-line star integrated flux densities function (Figure 11) resembles that of the candidate post-AGB stars at the faint end. At the bright end, however, there is a clear excess of emission-line stars over PNe/post-AGB candidates. Given that the H II sources within this compilation of 114 radio sources also often had emission-line stars associated with them, it is likely that those bright emission-line stars are massive stars. It is not clear whether these are young or evolved, but one could speculate that young sources are more often

Table 3. Example of ASKAP 888 MHz radio detections within 10 arcsec of sources at one time classed as potential PNe. The positions are those of the radio source, and the distance (Δ) is that between the radio source and the coordinates listed in Simbad. The most likely classes are Planetary Nebula (PN), candidate post-AGB object (pAGB), emission-line star (em*), Young Stellar Object (YSO) or H II region (H II). See comments where there is doubt. The full table is available online in the supplementary material.

Name	EMU ID	RA (J2000) h m s	Dec (J2000) ° ' "	— peak —		— integrated —		Δ "	Class	Comments
				F (mJy)	σ (mJy)	F (mJy)	σ (mJy)			
SMPLMC 104	EMU ES J042437.3–694221	04 24 37.4	–69 42 21	0.31	0.06	0.34	0.06	0.9	PN?	
SMPLMC 6	EMU ES J044738.8–722821	04 47 38.8	–72 28 21	0.80	0.05	0.78	0.05	0.9	PN	
SMPLMC 5	EMU ES J044808.4–672606	04 48 08.4	–67 26 07	0.39	0.05	0.34	0.04	0.7	pAGB	
SMPLMC 7	EMU ES J044829.6–690813	04 48 29.6	–69 08 13	0.45	0.05	0.48	0.05	0.5	PN	
SMPLMC 10	EMU ES J045108.7–684904	04 51 08.7	–68 49 05	0.45	0.05	0.47	0.05	1.3	PN	
Sk –70 10	EMU EC J045325.9–703541	04 53 25.9	–70 35 42	0.44	0.09	1.45	0.30	3.1	H II	Contains BO III[e]
...										

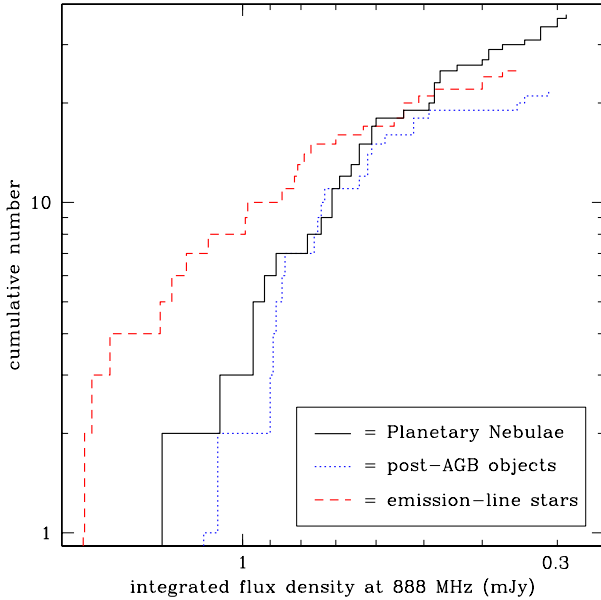


Figure 11. Cumulative 888 MHz flux distributions of planetary nebulae, post-AGB objects and emission-line stars.

associated with extended radio emission from an H II region and evolved stars are more often isolated and thus unresolved. This is somewhat corroborated by the fact that of all stars with supergiant luminosity class (I or II, according to Simbad), five are unresolved by ASKAP and only one is found in extended radio emission, versus a ratio of 20:11 for luminosity classes III–V. Forbidden line emission ("[e]") is marginally more prevalent among unresolved radio sources (15 out of 27) as well, compared to stars associated with extended radio emission (5 out of 11).

4.2 Young stellar objects

YSOs become radio continuum sources once they ionize a sufficient amount of gas and free-free emission yields a relatively flat continuum emission spectrum extending from the near-IR far into the radio regime. They are also found in complex star-forming regions that are often embedded in H II regions that exhibit bright free-free radio emission. As seen in the previous section, some YSOs have been mistaken for PNe. We here examine the ASKAP radio detections of a small sample of particularly well characterised YSOs from the

groundbreaking *Herschel Space Observatory* spectroscopy sample of Oliveira et al. (2019).

Of the seventeen YSOs (within the LMC), three had initially been associated with one compact region of star formation and would be blended in our radio survey. These were not detected; among the remainder, nine were detected (within a search radius of 10 arcsec; all were found within ≤ 6 arcsec) including all three YSOs from the unique star-forming region LHA 120-N 113 in which complex organic molecules were discovered with the Atacama Large (sub-)Millimetre Array (ALMA) by Sewilo et al. (2018). Table 4 lists their properties. They span a range in radio integrated flux densities from 0.45 to 47 mJy, and all but two are brighter than the PNe distribution (Figure 11). Because they are among the more extremely luminous, massive and consequently radio brighter YSOs they appear relatively isolated and unresolved against the ambient emission, except for two clearly extended sources both in the LHA 120-N 44 region.

The most striking result is the sharp-cut division between those YSOs detected with ASKAP and those not, in terms of the measurement of the gas temperature based on far-IR emission lines of CO detected with *Herschel* (Oliveira et al. 2019, their Table 6). All sources with temperatures $T > 700$ K are detected, and all sources with $T < 700$ K are not. This suggests a strong relation between the line emission from the photo-dissociation regions at the interfaces of neutral and ionized gas, and the free-free emission from the ionized regions surrounding the nascent, presumed massive O-type stars. The brightest radio source, LHA 120-N 113 YSO-4 did not have a temperature determined from CO but it is one of the two brightest [O III] 88 μ m emitters (Oliveira et al. 2019) and thus hosts a highly ionized compact or ultra-compact H II region.

4.3 Novæ and supernovæ

Of 46 novæ listed in Simbad within the ASKAP footprint, two are recovered in our ASKAP catalogue (both in the GOLD list) within $\sim 2''$: Nova LMC 1988 b ($F_{888} = 2.81 \pm 0.06$ mJy) and Nova candidate LHA 120-S 162 ($F_{888} = 0.46 \pm 0.05$ mJy). While the latter was designated Nova LMC 2001 it is a Galactic mid-M type main-sequence emission-line star (Morgan et al. 1992; Shafter 2013). The former, Nova LMC 1988 b was a fast nova and the first neon nova discovered in the LMC (Sekiguchi et al. 1989). This implies the eruption occurred on a massive O–Ne–Mg white dwarf. Neon novæ are energetic and not rare, so it is not immediately clear why this should have been the only nova detected with flux density > 0.5 mJy.

SN 1987A is detected as a bright point source, with $F_{888} =$

Table 4. ASKAP 888 MHz radio detections within 10 arcsec of sources from the *Herschel* spectroscopy of the YSO sample (Oliveira et al. 2019). The names are as in (Oliveira et al. 2019), the positions are those of the radio source, and the distance (Δ) is that between the radio source and the YSO coordinates (IR-based).

Name	EMU ID	RA (J2000) h m s	Dec (J2000) ° ' "	— peak — F (mJy) σ (mJy)	— integrated — F (mJy) σ (mJy)	Δ "	Comments
IRAS 04514–6931	EMU ES J045111.7–692647	04 51 11.7	–69 26 48	0.50 0.07	0.45 0.06	1.9	
LHA 120-N 113 YSO-1	EMU EC J051317.6–692223	05 13 17.6	–69 22 24	39.0 0.6	44.5 0.6	1.2	
LHA 120-N 113 YSO-4	EMU EC J051321.4–692239	05 13 21.4	–69 22 40	40.7 0.6	47.0 0.7	1.9	
LHA 120-N 113 YSO-3	EMU EC J051324.7–692245	05 13 24.8	–69 22 46	11.2 0.6	14.2 0.7	2.0	
SAGE 051351.5–672721.9	EMU ES J051351.4–672719	05 13 51.4	–67 27 19	3.37 0.17	4.53 0.24	2.8	
SAGE 052202.7–674702.1	EMU ES J052202.7–674658	05 22 02.7	–67 46 59	1.20 0.06	3.8 0.2	3.4	extended
SAGE 052212.6–675832.4	EMU EC J052213.3–675834	05 22 13.4	–67 58 34	30.2 1.1	72.4 2.8	04.7	extended
SAGE 053054.2–683428.3	EMU ES J053054.5–683422	05 30 54.6	–68 34 23	9.17 0.08	14.90 0.13	6.1	
ST 01	EMU EC J053931.0–701216	05 39 31.0	–70 12 16	2.43 0.08	3.18 0.11	1.1	

1.1432 \pm 0.0013 Jy. It is listed as EMU ES J053527.8–691611 in the BRONZE source list. Its proximity to 30 Doradus prevented its original inclusion in the catalogue due to the complexity of the surroundings even though SN 1987A itself stands out clearly; it was reinstated subsequently. The radio emission primarily arises from the 1''6-diameter torus, which was resolved at 92 GHz for the first time by Lakićević et al. (2011). The integrated flux density at 888 MHz have continued to increase by \sim 27 per cent since 2013–2014 when it was \approx 0.90 Jy (Callingham et al. 2016), but at the slower pace observed after an initial exponential growth until 2009 (day \sim 8000, Ng et al. 2013).

While radio detections are made at the locations of at least two dozen SNe in background galaxies, in none of the cases could we unequivocally ascribe the radio emission to the SN and in most cases the host galaxy dominates.

4.4 Supergiants

Various classes of massive supergiant stars could be detectable at low radio frequencies, including Luminous Blue Variables (LBVs), Wolf–Rayet (WR) stars – especially if in colliding-wind binaries – and Be or B[e] stars (massive B-type stars showing permitted emission lines from an accretion disk and/or forbidden emission lines from a more tenuous envelope, respectively).

Nine such sources from the far-IR study of van Loon et al. (2010) were pursued, resulting in the detection of four of these: (a) the dusty B[e] star IRAS 04530–6916 (van Loon et al. 2005) seen on the image as a point source with a peak flux density \sim 0.9 mJy⁷ though it had not made the cut for the catalogue, (b) the Of/O?p–WR transition object Brey 3 (IRAS 04537–6922; Heydari-Malayeri & Melnick 1992) at $F_{888} = 5.25 \pm 0.06$ mJy, (c) emission-line object IRAS 05047–6644 at $F_{888} = 12.27 \pm 0.06$ mJy and (d) IRAS 05216–6753 at $F_{888} = 3.77 \pm 0.11$ mJy – likely a massive early-type star illuminating a dusty envelope (Chen et al. 2009). It is likely the nature of the 888 MHz radiation mechanism in these sources is free–free emission from ionized circumstellar gas.

LBV S Dor may have been detected as a point source with a peak flux density \sim 0.19 mJy, but it is blended with much brighter adjacent emission from the N 119 H II region. The radio emission near R 71, at \sim 12 arcsec distance (\sim 3 pc at the distance of the LMC) to the South–West in an otherwise sparse field, is unresolved and peaks at \sim 0.21 mJy. R 71 had also not been detected within a

3σ level of 24 μ Jy at 5 GHz in 2015 (Mehner et al. 2017). While no circumstellar nebula appears to be present around R 71 (based on HST H α imaging before the recent eruption of R 71), there is a hint for a very small (less than 1 arcsec or 0.25 pc) circumstellar nebula around S Dor due to the [N II] emission lines detected in a long-slit échelle spectrum (Weis 2003). Unfortunately, the possible nebula is not detected in HST H α imaging (Weis 2003).

LBV nebulae have been detected at higher radio frequencies before, for instance, R 127, R 143, S 61 and S 119 (Agliozzo et al. 2012, 2017a,b, 2019). Cross-matching these sources with the ASKAP LMC 888 MHz catalogue revealed integrated fluxes for R 127 (EMU ES J053643.4–692947) of $F_{888} = 2.69 \pm 0.18$ mJy, S 61 (EMU EC J054551.8–671426) of $F_{888} = 2.31 \pm 0.06$ mJy and S 119 (EMU ES J053125.5–690537) of $F_{888} = 1.09 \pm 0.11$ mJy, all point-like sources.

4.5 X-ray binaries

Simbad lists 66 X-ray binaries within the ASKAP footprint. With the only exception of LMC X-2 (a low-mass X-ray binary), these are high-mass X-ray binary (HMXB) systems formed by a compact object (in most cases a neutron star) accreting matter from a massive companion star (Antoniou & Zezas 2016). From about 20 systems X-ray pulsations were discovered, which identify the spin period of the neutron star. In many of the others cases the nature of the X-ray source is less clear; low statistical data quality and/or uncertain X-ray position do not allow identification of the optical counterpart.

Four of the 66 (candidate) X-ray binaries were successfully recovered in the 888 MHz catalogue – three in the GOLD and one in the SILVER source list. They are all well detected, coincident and isolated in the radio.

The radio-brightest of the four at $F_{888} = 9.15 \pm 0.05$ mJy correlates with RX J0457.2–6612, a little-known X-ray source, listed in the ROSAT PSPC X-ray catalogue of the LMC region by Haberl & Pietsch (1999a) and proposed by Kahabka (2002) as X-ray binary. However, there is no star within 20'' brighter than $V = 18.8$ mag, which most likely excludes an HMXB nature. The X-ray source is probably identified with a QSO listed in Bailer-Jones et al. (2019), which is further supported by the ASKAP radio detection.

The second brightest (EMU ES J050123.5–703329, $F_{888} = 3.25 \pm 0.05$ mJy) coincides with *Einstein* source Cal 9 (Cowley et al. 1984), which was identified with ROSAT source RX J0501.6–7034 by Schmidtke et al. (1999). The authors list as possible optical counterpart HV 2289 – an early-B type supergiant with an orbital period of $P = 6.94$ d (Bianchi & Pakull 1984). X-ray positions from Ein-

⁷ radio emission had been detected by Filipovic et al. (1995)

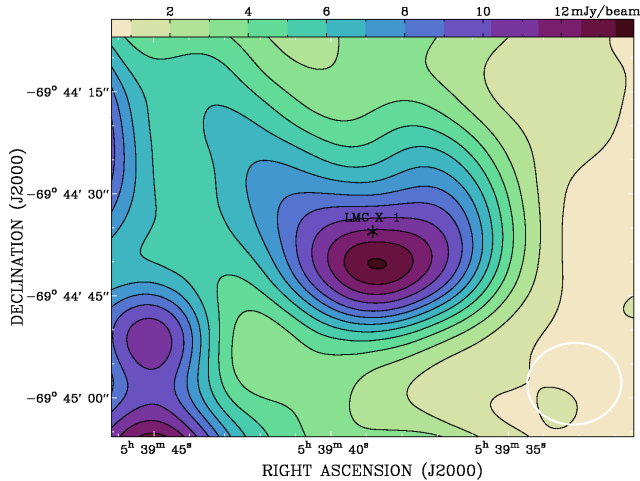


Figure 12. X-ray binary LMC X-1 seen in the focus of a radio arc in the 888 MHz ASKAP LMC image. The beam size for ASKAP 888 MHz is $\sim 13''.9 \times 12''.1$ and is represented by the white ellipse in the bottom right.

stein and ROSAT are not precise enough to allow a secure optical identification, but the source was also detected by XMM-Newton (4XMM J050123.3–703333 in the 4XMM-DR9 catalogue; Webb et al. 2020) with a position error of $1''.5$ (1σ). This position is $2''.4$ from the Gaia DR2 position (Gaia Collaboration et al. 2018b) of HV 2289, consistent within the uncertainty. Also the radio position is consistent within errors with the 4XMM source. Neuguera & Coe (2002) give B0 Ve for the spectral type, which suggests a classical Be/X-ray binary instead of a supergiant system. On the other hand, the orbital period of 6.94 d would be too short for a Be/X-ray binary (e.g., Haberl & Sturm 2016) and favour a supergiant system. The radio detection of this system makes it even more puzzling.

The two faintest radio detections are associated with RX J0535.8–6530 ($F_{888} = 0.57 \pm 0.05$ mJy) and [SG2005] LMC 15 (0.40 ± 0.05 mJy). The former was found to be a variable X-ray source by Haberl & Pietsch (1999b); an optical counterpart was suggested to be a star by Grazian et al. (2002), and it is also detected with Spitzer and WISE. The GLADE catalogue (Dályá et al. 2018) and Bailer-Jones et al. (2019) list a background galaxy with redshift 0.05. The radio detection supports this identification.

The latter, [SG2005] LMC 15 was proposed as an HMXB candidate by Shtykovskiy & Gilfanov (2005), but the optical counterpart is not coincident with the XMM-Newton and Spitzer source and the real counterpart of the X-ray and radio source is likely the QSO MQS J054433.81–682813.7 given in the Million Quasars catalogue (Milliquas V6.3, Flesch 2015).

The most famous X-ray binaries in the LMC, LMC X-1 (a black hole + supergiant system) and LMC X-4 (a neutron star accreting from a Roche-lobe filling supergiant) were not detected. However, we do detect a radio arc with LMC X-1 in its focus (Figure 12), peaking at $4''$ due South (1 pc in projection at the distance of the LMC). If this is a bow shock (Hyde et al. 2017) ahead of the supersonic motion of LMC X-1 then this means the binary must have originated from *outside* the prominent star-forming region LHA 120-N 159 into which it would seem to be heading. The system may have run away from N 159 and subsequently received a lateral kick when the supernova created the black hole.

4.6 Galactic active stars

Galactic stars seen in the direction of the Magellanic Clouds are at high Galactic latitude and radio-loud stars among them are most commonly nearby (~ 100 pc) flare stars (M-dwarves) or interacting tight binaries.

We detect the hierarchical young active system AB Dor (Pakull 1981; Collier Cameron et al. 1988; Wolter et al. 2014; Azulay et al. 2015, 2017) and resolve the emission coming from the main (K-type) component and the B component (Figure 13) – the latter of which itself is a spectroscopic M-dwarf binary. White et al. (1988) had ruled out 8-GHz emission coming from component B, but the system was later resolved at 5 GHz by Beasley & Cram (1993) and Lim (1993), with the latter work showing the highly polarized and variable nature of component B. The system has another component, C, which is a late-M dwarf with a sub-stellar companion (Climent et al. 2019) close to the main component but on the side of component B, so we cannot discard the possibility that some of the radio emission originates from it. The ASKAP emission is heavily blended, with a peak and integrated flux density of $F_{888,\text{peak}} = 2.80 \pm 0.05$ mJy and $F_{888,\text{total}} = 3.57 \pm 0.07$ mJy, respectively. Slee et al. (1984) detected it at 5 GHz (5.2 mJy); Vaughan & Large (1986) subsequently detected it at 843 MHz at a similar level (4 mJy) and our measurement confirms the flat spectrum (in F_ν). Collier (1982) characterised its activity as that of an FK Com system, which is associated with rapid rotation and evolution off of the main sequence (Oliveira & Foing 1999). Rucinski (1983), however, argued for youth and a post-T Tauri status and their detection of lithium seemed to prove that. Innis et al. (1986) (see also Ortega et al. 2007) determined the association of the AB Dor system with the Pleiades moving group (later revisited as the AB Dor moving group – see, e.g., Barenfeld et al. 2013), confirming its relative youth. The activity of AB Dor is usually associated with coronal, magnetic activity (e.g., Donati & Collier Cameron 1997; Donati et al. 1999; Jardine et al. 2002; Sanz-Forcada et al. 2003). AB Dor is at the same distance of 15 pc as the eruptive pair of M dwarves CD –38° 11343, which was detected with ASKAP by Riggi et al. (2021) at essentially the same integrated radio flux densities (at 912 MHz) as AB Dor.

The RS CVn system AE Men is detected, at $F_{888} = 1.51 \pm 0.06$ mJy. At a Gaia distance of $d = 288$ pc this corresponds to a radio luminosity of 2×10^{17} erg s^{-1} Hz^{-1} , placing it among the top 10 per cent integrated radio flux densities of this kind of system (Morris & Mutel 1988; Güdel 2002). This system is of K2 III+F/G spectral type and it is suggested to exhibit non-thermal (gyrosynchrotron) emission. What makes this object unusual compared to the $\sim 100+$ known population of RS CVn type systems is its X-ray (ROSAT), $H\alpha$ and especially IR (AllWISE) detection. AE Men was observed on several occasions with MOST and ATCA (Slee et al. 1987; Vaughan & Large 1987; Wendker 1995) but this is its first radio continuum detection. We reprocessed the ATCA observations from 1994 and confirm that it was not detected.

The β Lyrae-type eclipsing binary BK Dor (= CD –67° 435) is also detected for the first time at radio frequencies, with $F_{888} = 0.90 \pm 0.07$ mJy. With the Gaia distance of 279 pc this yields a radio luminosity of 8×10^{16} erg s^{-1} Hz^{-1} , not as high as AE Men but still luminous. It was discovered as a variable X-ray source by Fuhrmeister & Schmitt (2003) before being associated with the G7 III star by Torres et al. (2006) and found to be a short-period ($P = 2.2$ d) eclipsing binary by Szczygiel et al. (2008). In such a system the two stars are highly distorted and exchange mass.

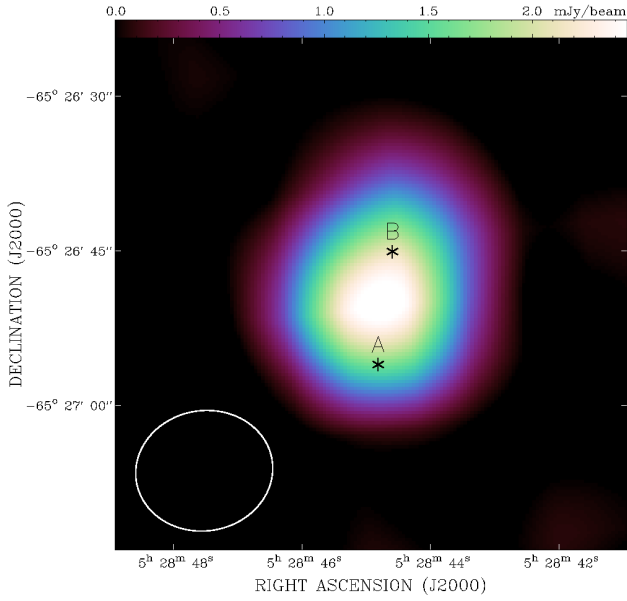


Figure 13. LMC AB Dor, a hierarchical young active system detected in the 888 MHz ASKAP LMC image where emission coming from the main component and the B component contribute. ASKAP 888 MHz beam size is $\sim 13''.9 \times 12''.1$, represented by the white ellipse in the bottom left.

5 BACKGROUND SOURCES

Here we discuss the extragalactic sources seen behind the LMC, which dominate the source counts. The radio emission from these sources is due to synchrotron radiation from relativistic electrons in magnetic fields and free-free emission from H II regions.

5.1 Radio galaxies

The ASKAP LMC image features some spectacular radio galaxies, showcasing a clearer morphology of these sources than has been seen before. Figure 14 shows a few examples of these radio systems.

Figure 14, (a). The NW quadrant shows a Fanaroff–Riley II (FR II) system (Fanaroff & Riley 1974), which are luminous radio systems brighter near their extremities than near their centres. This is a known radio source, PMN J0449–7219 (Filipovic et al. 1998d) and is seen as three islands (islands 14012, 13945 and 13724) in our ASKAP catalogue. The jets originate from galaxy WISEA J044917.77–721843.7 (a.k.a. 2MASS-6X J04491744–7218434, VISTA J044917.454–721843.85) for which Bilicki et al. (2016) give an extinction-corrected R-band magnitude of 19.62 and a photometric redshift of 0.47. With a radio size of $5''.5$, this makes it a giant radio galaxy of projected linear size of ~ 1.9 Mpc. A similar source in the SE corner of the image is most likely hosted by the galaxy VISTA J045013.036–722036.25 ($K_{sp} = 15.45$ mag, a.k.a. WISEA J045013.00–722036.0, 2MASS-6X J04501307–7220362), for which Bilicki et al. (2016) give an extinction-corrected R-band magnitude of 19.68 and a photometric redshift of 0.35. With a radio size of $3''.4$, this makes it another giant radio galaxy of projected linear size of ~ 1.0 Mpc. Whilst the radio emission from the ends of the jets can be seen in the SUMSS 843 MHz image, the fainter, central part of this source, where the radio jets most likely originate, has not been seen before.

Figure 14, (b). This is likely a wide-angle tailed (WAT) radio galaxy hosted by LEDA 257123 (EMU EC J043753.4–731437),

one of the members of galaxy cluster Abell S0485 with a mean spectroscopic redshift of 0.061 based on seven galaxies from the 6dF redshift survey (Jones et al. 2009). Neither the host galaxy of the WAT nor LEDA 257043 (EMU EC J043740.1–731508) or [CAC2009] S0485 b (a.k.a. 2MASX J04373976–7315056), apparently superposed on the SW tail of this WAT, have a spectroscopic redshift, and the host galaxy LEDA 257123 is not among the three brightest galaxies (Coziol et al. 2009). Assuming the cluster redshift for the host, the radio size of the WAT of $6''.2$ corresponds to a projected linear size of 440 kpc.

Figure 14, (c). ASKAP 888-MHz image reveals that this known radio source (PMN J0603–7325) has an S-shaped morphology indicating precessing jets. The strong radio core is coincident with the galaxy 2MASX J06030694–732529 (EMU EC J060306.4–732529) for which Bilicki et al. (2016) give a corrected R-band magnitude of 16.32 and a photometric redshift of 0.156. With an angular extent of $3''.5$ this corresponds to a projected linear size of 570 kpc.

Figure 14, (d). This radio source (PKS 0458–720, PMN J0458–7156, EMU EC J045804.2–715635) shows an even more extreme S-shape likely due to projection along the line of sight. Its radio core coincides with 2MASX J04580433–7156347 (a.k.a. SMSS J045804.30–715635.0, $r_{\text{Petro}} = 17.07$ mag, Wolf et al. 2018), but no (photometric) redshift is available.

These galaxies provide examples of the potential for exploring the morphologies in greater detail than previously, and for locating the host galaxies of these extragalactic marvels. We provide more in-depth analysis using high-resolution IR images and optical spectroscopy in a followup paper (Pennock et al., in prep.).

5.2 Comparison with the GLEAM 4-Jy sample

The Galactic and Extragalactic All-sky MWA 4-Jy sample (G4Jy; White et al. 2020a,b), from the Murchison Widefield Array (MWA), provides flux-densities across the range 72 to 231 MHz at DEC $< 30^\circ$. G4Jy is a complete sample of the brightest radio sources, $F > 4$ Jy, which are expected to be mainly AGN with powerful radio-jets (strong optically-thin synchrotron emission). Six of the sources from this sample lie within the ASKAP LMC field, all of which were detected in the ASKAP observations. These are shown in Figure 15 and show the large improvement the ASKAP image offers in resolution, which allows the identification of the optical/infrared counterpart of these radio sources, and while almost all host galaxies are identified in the WISE image, some are very faint. These GLEAM sources, which appear at first glance to be one source, are revealed to be multiple sources by ASKAP. The majority of these sources have the appearance of FR II sources. For the sources G4Jy 482, G4Jy 553 and G4Jy 596, ASKAP shows that they are double sources not resolved in SUMSS.

Figure 15, top-left. Contours of G4Jy 595 (a.k.a. GLEAM J060849–655110) from ASKAP reveal that the tear drop shaped radio source seen in GLEAM is in fact two sources. The southern source is an extreme bent tailed source hosted by the galaxy 2MASX J06085498–6552559 (a.k.a. WISEA J060854.94–655255.6) with $z = 0.03752$ (Jones et al. 2009). The northern one is a radio point source hosted by the galaxy ESO 086-G062 (a.k.a. WISEA J060852.00–654350.2), with $z = 0.037$ (Wegner et al. 2003), which appears to be part of a galaxy group that the bent tailed radio source has moved through. In fact, Saulder et al. (2016) lists the group of three galaxies 2MRS 3198 at $z = 0.03774$. The third member galaxy is 2MASX J06090657–6544539 (a.k.a. LEDA 310538) with $z =$

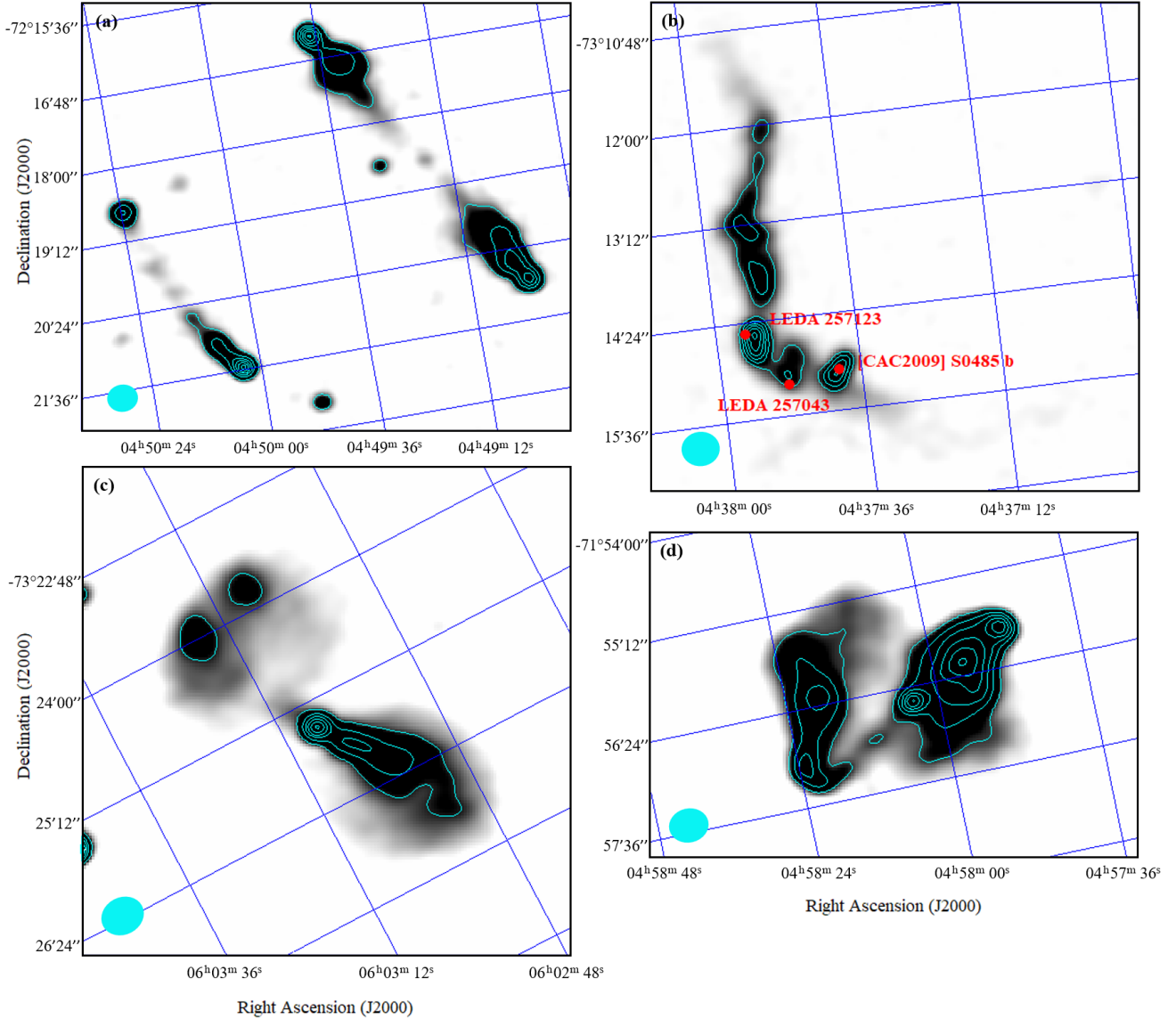


Figure 14. Four examples of radio emission from galaxies. The structure of the four radio sources is shown by the cyan contours that are drawn at equally spaced values in brightness. The beam size for ASKAP 888 MHz is $\sim 13''.9 \times 12''.1$, which is represented by the cyan ellipse. (a) Two examples of jets originating from a less bright central source (FR II systems) where contours span from $0.2\text{--}29 \text{ mJy beam}^{-1}$. (b) Galaxy cluster at $z \sim 0.06$. Low surface brightness at lower right is $0.25\text{--}0.45 \text{ mJy beam}^{-1}$. The contours span from $0.2\text{--}19 \text{ mJy beam}^{-1}$. (c) A jettted system that reveals interesting morphology in the jets. Contours span from $3.7\text{--}28 \text{ mJy beam}^{-1}$. (d) A central radio source from which two jets originate. These jets are bent as they come into contact with the intra-cluster medium. The contours span from $3\text{--}19 \text{ mJy beam}^{-1}$.

0.03828 (Huchra et al. 2012), which lies $\sim 2'$ SE of ESO 086-G062 and is also detected as a radio point source.

Figure 15, top-right. ASKAP reveals that G4Jy 453 (GLEAM J042358–724601) comprises multiple sources. The western-most ASKAP radio source features an X-shaped radio galaxy known as PKS 0424–728 at a redshift of ~ 0.19 (inferred from photometry; Subrahmanyan et al. 1996). With more recent photometric redshifts of 0.229 and 0.214 from Bilicki et al. (2014) and Bilicki et al. (2016) its angular size of $4'.3$ gives it a projected linear size of 880 kpc. An unresolved source at 888 MHz is hosted by WISEA J042434.02–724241.3 with an even fainter 888 MHz source $\sim 24''$ SW with no optical/IR counterpart and the X-ray source 1RXS J042432.7–724253 in between them. The central source is revealed as a double radio source of size $\sim 33''$ hosted by WISEA J042501.60–724700.3 with no optical counterpart. Two ASKAP point sources at the E edge of the radio com-

plex can be identified with WISEA J042549.29–724330.8 (NE) and WISEA J042600.47–724828.9 (SE).

Figure 15, middle-left. This is G4Jy 587 a.k.a. PKS 0602–647 or GLEAM J060239–644324. At the centre of this radio structure is a pair of galaxies, the brighter of which, LEDA 319866 with $z = 0.045$ (Burgess & Hunstead 2006), is likely the host. Nearby galaxies with known redshifts show similar redshifts, such as the galaxy NW of the host that lies on the edge of the ASKAP contours, which is 2MASX J06023279–6442344 with $z \sim 0.048$ (photometric; Bilicki et al. 2014).

Figure 15, middle-right. The central source is G4Jy 482 (GLEAM J043709–645853) and the NE source is GLEAM J043738–645400 (not in the G4Jy sample). The former is MRC 0436–650 a.k.a. PKS 0436–650 hosted by the galaxy DES J043708.39–645901.9 ($r = 17.97$ mag, $z_{\text{sp}} = 0.360$, Burgess & Hunstead 2006). The NE double source is hosted by the QSO

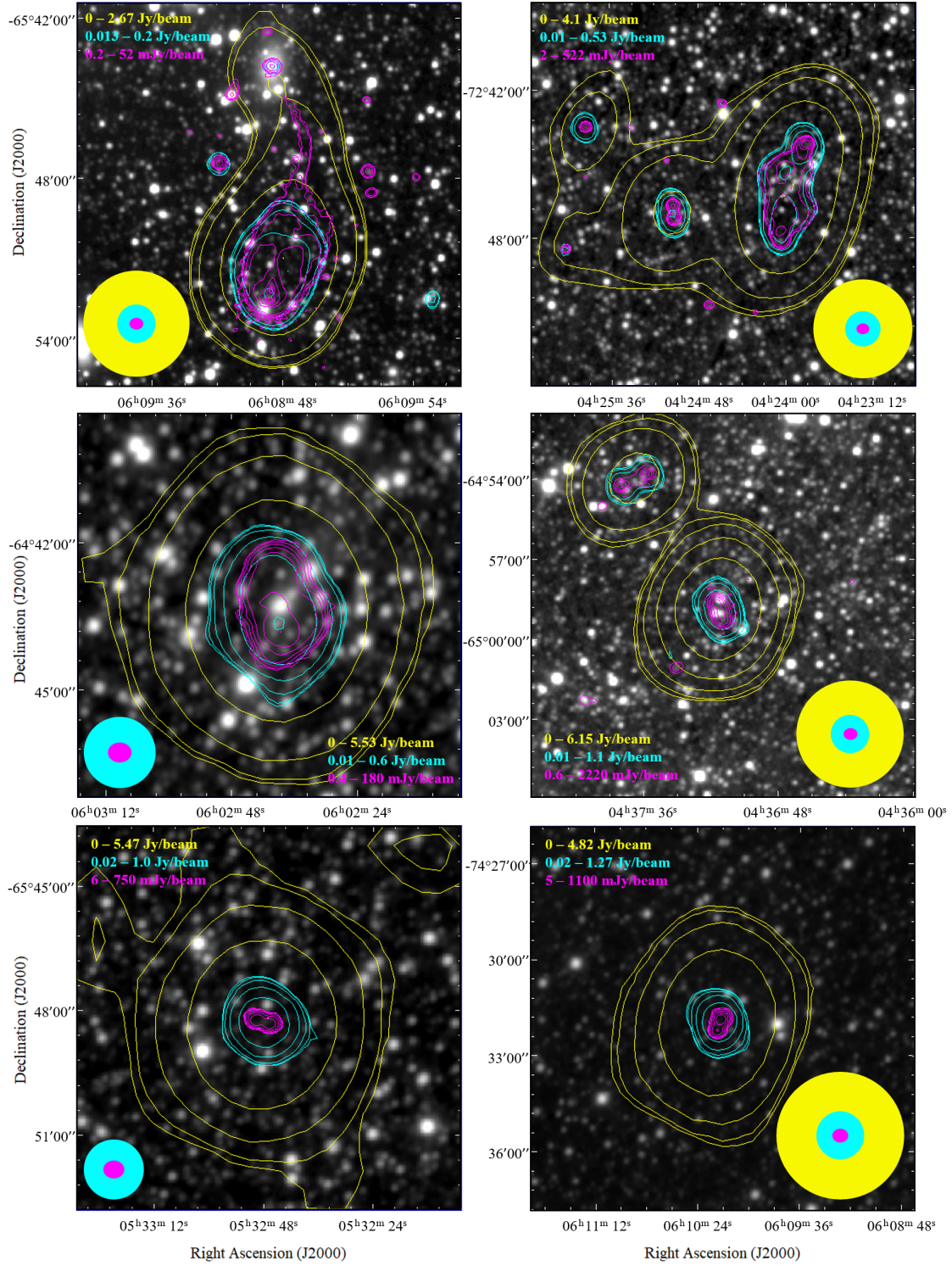


Figure 15. Comparison between ASKAP (magenta contours), SUMSS (cyan contours) and GLEAM (yellow contours) that represent logarithmically spaced brightness levels in the ASKAP image, the minimum and maximum of which are annotated in their respective colour. The background image is the WISE W3 band. The beam size for ASKAP 888 MHz is $\sim 13''9 \times 12''1$ and is represented by the magenta ellipse. The beam size for SUMSS 843 MHz is $\sim 43'' \times 43''$ and is represented by the cyan circle. The beam size for GLEAM 72–231 MHz is $\sim 2'' \times 2''$ and is represented by the yellow circle. The sources are (top-left) G4Jy 595, GLEAM J060849–655110, (top-right) G4Jy 453, GLEAM J042358–724601, (middle-left) G4Jy 482, GLEAM J043709–645853, (middle-right) G4Jy 587, GLEAM J060239–644324, (lower-left) G4Jy 553, GLEAM J053248–634820 and (lower-right) G4Jy 596, GLEAM J061014–743159.

candidate DES J043738.82–645402.1 ($r = 21.53$ mag, no z_{phot} available, [Abbott et al. 2018](#)) a.k.a. CWISE J043738.83–645402.0 ([Marocco et al. 2021](#)). The source ~ 2.7 SE of G4Jy 482 is DES J043724.19–650105.6 a.k.a. WISEA J043724.19–650104.9 with high stellarity, i.e. likely a QSO.

Figure 15, lower-left panel. The central source is G4Jy 553 (GLEAM J053248–634820), also known as PKS 0532–638 and MRC 0532–638 or ATPMN J053246.7–634820 ([McConnell et al. 2012](#)), hosted by the QSO candidate SMSS J053247.95–634818.1 ($g_{\text{Petro}} = 19.89$ mag, [Wolf et al. 2018](#)) a.k.a. WISEA J053247.87–634816.7 with typical QSO colors ($W12 \sim 1.0$ mag, $W23 \sim 3.0$ mag), suggesting a redshift of $z > 1$ (see e.g., [Fig. 2 of Krogager et al. 2018](#)).

Figure 15, lower-right panel. This is G4Jy 596 (GLEAM J061014–743159, PKS 0611–745), which was identified by [White et al. \(2020a\)](#) with WISEA J061013.90–743201.6 and is not detected in the optical.

5.3 IR properties of radio sources

The AllWISE catalogue ([Cutri et al. 2013](#)) is a well-explored all-sky survey with photometry from 3.35 to 22.1 μm . This wavelength regime allows for a selection of both obscured and unobscured AGN, which makes it a great catalogue to cross-match to discover extragalactic sources. Selection criteria for different types of AGN/galaxies are well documented (e.g., [Wright et al. 2010](#); [Jarrett et al. 2011](#); [Mateos et al. 2012](#); [Stern et al. 2012](#); [Assef et al. 2013](#); [Nikutta et al. 2014](#)) and the criteria from [Wright et al. \(2010\)](#) will be used here to discuss the radio population.

Cross-matching the AllWISE catalogue with the new ASKAP catalogue with a search radius of 5 arcsec and a maximum magnitude error in the W1 (3.4 μm), W2 (4.6 μm) and W3 (12 μm) bands of 0.2 mag yielded a total of 14,333 sources (combined GOLD and SILVER, which contain 7,413 and 6,920 sources, respectively). This search radius was used as the density of coincidences drops off sharply, approaching that of chance coincidences (tested by applying a large offset in RA and DEC and then cross-matching again) beyond a search radius of 5 arcsec, and coincidences found between 6–10 arcsec of stellar sources (including PNe) almost invariably turned out to be implausible associations. As a comparison with ASKAP detected sources, the sources within the LMC field that had no ASKAP detection (no ASKAP emission above 5σ of the local RMS) within 5 arcsec were considered. This amounted to 253,533 AllWISE non-ASKAP detected sources.

We plotted the ASKAP detections and non-detections on the W1–W2 vs. W2–W3 colour–colour diagram ([Figure 16](#)), based on [Figure 12 of Wright et al. \(2010\)](#). The majority of the radio detections are extragalactic sources. The stellar AGB sequence seen in the non-ASKAP detected diagram (right) is clearly not visible in the ASKAP detected diagram (left). The BRONZE source list also shows a similar colour–colour diagram to the combined GOLD and SILVER source lists and therefore the majority of sources are extragalactic.

Where LMC ISM dust emission affects the WISE detections it would also be too bright at radio frequencies. Extinction caused by dust within the LMC would affect the optical brightness of background AGN and galaxies. The vast majority of the ASKAP field is affected only by low or modest levels of such extinction ($A_V \ll 1$ mag), judging from extinction maps such as those produced by [Skowron et al. \(2020\)](#), which would not cause major difficulties for optical spectroscopy and certainly not lead to any

Table 5. Classifications of known AGN that have been detected with ASKAP and those that have not. Q = QSO, type-I broad-line core-dominated; A = AGN, type-I Seyfert/host-dominated; B = BL Lac object; N = narrow-line AGN (NLAGN), type-II Seyfert/host-dominated (includes unknown number of legacy narrow emission line galaxies (NELGs)/emission line galaxies (ELGs)/ low-ionization nuclear emission-line region (LINERs)); R = radio associated; X = X-ray associated.

	Total	A	Q	N	B	R	X
Radio	202	67	117	5	1	12	48
Non-radio	453	80	368	5	0	0	110

bias between the extragalactic populations with and without such spectroscopy.

5.3.1 Spectroscopic AGN

There are 657 spectroscopically observed AGN, from the milliquas catalogue of [Flesch \(2019a,b\)](#), in the field of the ASKAP LMC image. The highest contributions are from [Kozłowski et al. \(2012, 2013\)](#), [Geha et al. \(2003\)](#), [Esquej et al. \(2013\)](#) and [Ivanov et al. \(2016\)](#), contributing 547, 24, 23 and 10 objects, respectively.

This list of spectroscopically observed AGN was cross-matched with the combined GOLD and SILVER ASKAP LMC source lists with a search radius of 5 arcsec. This gave a total of 190 known AGN with radio detections, only 14 (< 8 per cent) of which had known radio detections prior to the present ASKAP observations. As expected, all known radio associated AGN are in the new ASKAP catalogue. The classifications of the known AGN that were radio detected and non-radio detected are described in [table 5](#).

The spectroscopically observed AGN have a selection bias. All had been chosen first and foremost because they are optically bright enough to take a spectrum of, which leads to a surplus of lower redshift AGN. Whether they are bright enough in the optical and a candidate AGN or not is determined from photometric surveys. The AGN has to dominate over the host to be selected as an AGN candidate, based on colour selections. If selected in the optical, where optical emission from AGN comes from the accretion disk and the broad line region (BLR), which introduces a bias towards unobscured AGN, typically type 1 AGN. IR provides a selection that is sensitive to both obscured and unobscured AGN, providing a more isotropic selection than in the optical. In this regime the dust obscuring the central AGN re-emits the absorbed optical emission into the IR. Most of the AGN behind the LMC were spectroscopically observed in the optical, even if they were selected in the IR, which lends the bias towards the more unobscured AGN yet again.

The redshifts of the known radio AGN range from $z = 0.001$ –3.46. The distribution of integrated radio flux densities for spectroscopically observed radio AGN compared to all radio sources (shown in [Figure 17 \(left\)](#)) reveals only a slight bias towards the brightest radio sources having more spectroscopic follow-up, which is not unexpected, since the radio brightness would have made them targets for spectroscopy. The slope of the histogram of flux density of known AGN detected is similar to the slope of the combined GOLD and SILVER source lists; below ~ 10 mJy the shape of the flux density functions are indistinguishable.

The redshift distributions for radio-bright, radio-faint and non-radio sources ([Figure 17 \(right\)](#)) are similar, with a slight bias towards lower redshift AGN being radio sources. While one might expect a bias towards higher redshift for radio sources compared to the overall distribution of galaxies, observational bias in

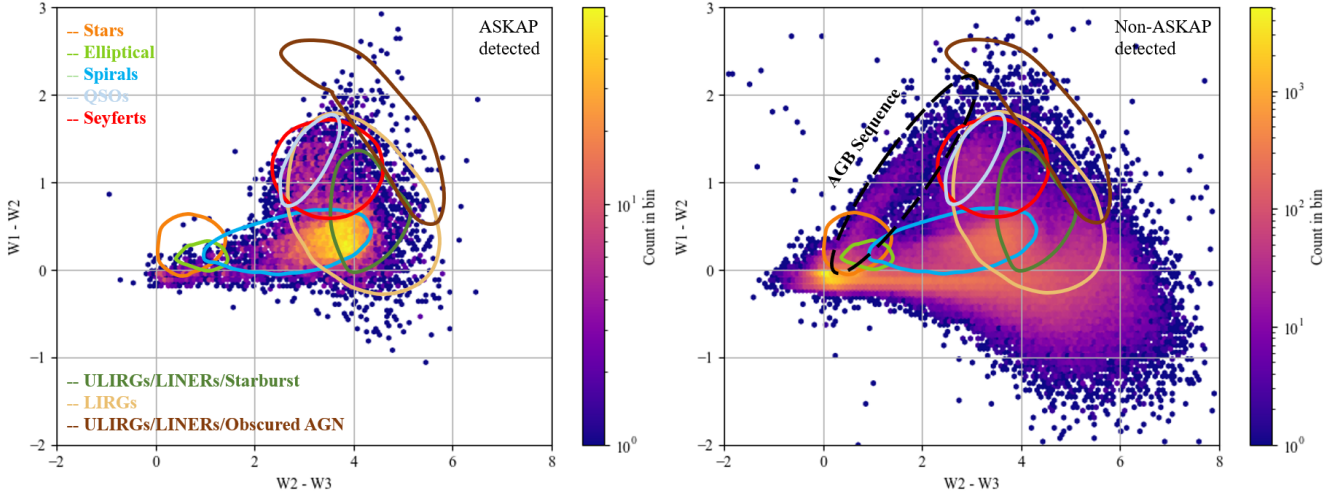


Figure 16. (Left) LMC AllWISE colour–colour diagram of the combined GOLD and SILVER source lists. (Right) LMC AllWISE colour–colour diagram of the non-ASKAP detected sources in the LMC field.

the spectroscopy most likely negates that. The SILVER source list ($F_{888} < 0.5$ mJy) overall redshift distributions seem to be half way between the GOLD source list ($F_{888} > 0.5$ mJy) distribution and the non-radio distribution. Non-radio detected spectroscopically observed AGN are generally at higher redshift, this could be because at higher redshift the optical will in fact be the UV restframe, thus making AGN brighter and easier to obtain an optical spectrum of. Furthermore, at higher redshift one gets a higher fraction of radio-quiet AGN, which will be detectable in the optical but too faint for ASKAP.

Figure 18 compares, using AllWISE colours, the radio and non-radio detected AGN. Radio detected AGN overall appear redder in W2–W3 than those not detected in radio. A Kolmogorov–Smirnov test of the radio and non-radio detected populations in the W2–W3 colour band shows that the radio detected population is redder at a significance level of 10 per cent⁸.

We compare the redshift distributions of ASKAP and non-ASKAP detected AGN using the same AllWISE colours as before and colouring based on redshift. (Figure 19) shows that both the detected and non-detected AGN show a general gradient in redshift as a function of WISE colour, with a few outliers.

Figure 20 (top-left & right) shows a WISE colour–colour diagram for the ASKAP detected sources and the known AGN in the GOLD and SILVER samples. Using the outlined regions for "QSOs" and "Spirals", in the GOLD list ~ 445 out of 4852 (~ 9.2 per cent) are predicted to be AGN (from AllWISE colours Wright et al. 2010) and in the SILVER ~ 270 out of 5050 (~ 5.4 per cent) are predicted to be AGN. As expected, there are more spirals compared to AGN in the SILVER list, since spirals tend to be star-forming and that is where the radio emission comes from, which tends to be fainter than the radio emission from an AGN and therefore a higher fraction of AGN are expected in the GOLD list.

The upturn towards the fainter flux densities at $F_{888} \sim 3$ mJy can be seen in the overall flux distribution (see Figure 6) representing the beginning of the faint galaxy population. We thus separated the catalogue into a bright sample ($F_{888} > 3$ mJy) and a faint sample ($F_{888} < 3$ mJy). Cross-matching this with the AllWISE catalogue

provides 806 and 13,414 sources, respectively, with a maximum magnitude error in the W1, W2 and W3 bands of 0.2 mag. In Figure 20 (lower panels) we plot these two samples on a colour–colour diagram, which shows the distributions of the source types in the bright and faint samples, with regions of expected classifications annotated. From the colours shown in the plots the number of spirals in the faint population is greater than the number of AGN, whereas in the bright sample the ratio of spirals to AGN is lower. As expected the spiral galaxies are more prevalent in the faint population. Cross-matching with the spectroscopically observed AGN list gives 123 radio-faint AGN and 24 radio-bright AGN. The fraction of AGN is larger in the bright sample (~ 3 per cent) than in the faint sample (~ 0.9 per cent) as expected.

6 SPECTRAL INDICES

We define the spectral index α by $F_\nu \propto \nu^\alpha$, where F_ν is the integrated flux density at frequency ν . A flatter spectral index close to zero indicates free–free emission, and a steep negative spectral index, ~ -0.7 , indicates synchrotron emission. Archival ATCA data at 1.384 GHz (Hughes et al. 2007) cover a similar area as the ASKAP image, though with a larger beam size of $40''$. We cross-matched the ASKAP LMC 888 MHz catalogue (GOLD, SILVER and BRONZE) with the ATCA 1.384 GHz source list described in Filipović (2021) with a search radius of $5''$. Limiting the sources to those with a ≤ 1 per cent error in ASKAP and ATCA integrated flux densities (determined by AEGEAN) provides 1,869 sources.

The histogram of spectral indices (Figure 21 (upper)) is dominated by an extragalactic population of synchrotron sources ($\alpha < 0$). This is confirmed by the small sample of 25 spectroscopically confirmed AGN – it is not unusual for some AGN to show a flatter spectrum or even to peak at a few GHz. On the other hand, two YSOs (SAGE 053054.2–683428.3 from Table 4, and [BE74] 615 from Table 3) and an H II region ([RP2006] 1933 from Table 3) have $\alpha \sim 0$ consistent with their free–free emission spectrum. The two "candidate PNe" (SMP LMC 32 and [RP2006] 338, Table 3) at $\alpha \sim -0.8$ are in fact among the few PN candidates that we had rejected on the basis of the large (in these cases $\sim 9''$) distance from the radio position – their synchrotron nature confirms that they are instead background sources.

⁸ the probability of the null hypothesis in the Kolmogorov–Smirnov test that these two samples are drawn from the same parent sample.

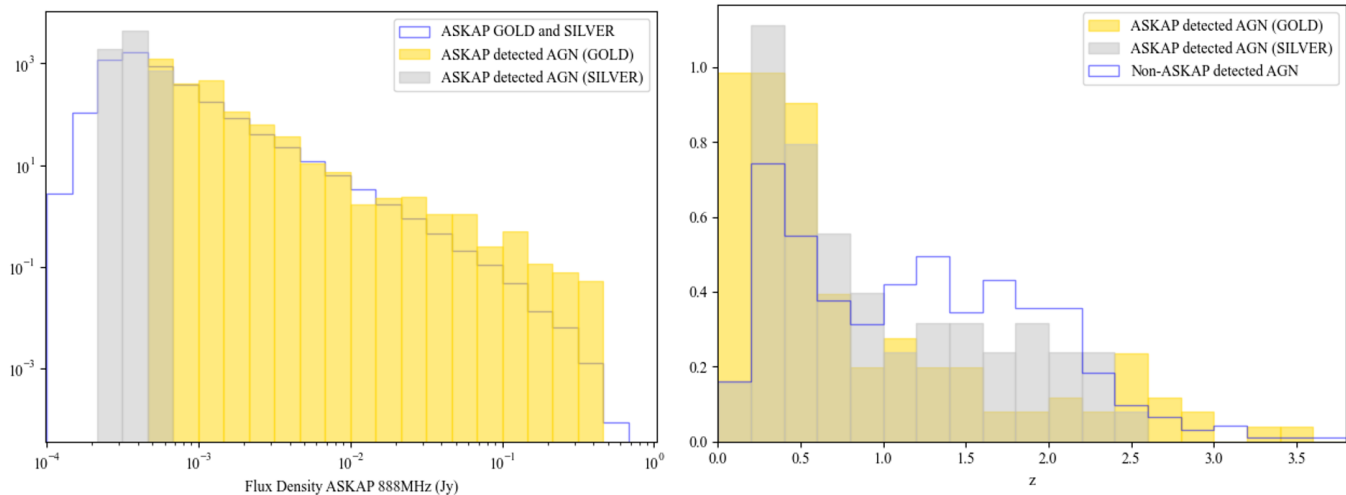


Figure 17. (Left) Normalised histogram comparing integrated flux densities of spectroscopically observed radio AGN vs. all radio AGN in the LMC field. This shows that the spectroscopically observed radio AGN tend to brighter flux densities than the overall radio population. (Right) Normalised histogram comparing the redshift of spectroscopically observed radio AGN (separated into GOLD and SILVER) vs. all spectroscopically observed AGN in the LMC field. This shows that radio-detected spectroscopically observed AGN tend more towards lower redshift compared to non-radio detected spectroscopically observed AGN.

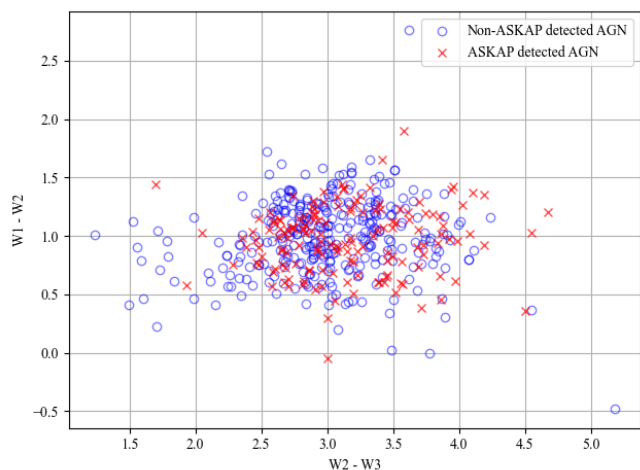


Figure 18. AllWISE colour–colour diagram of spectroscopically observed AGN, where those detected in the radio with ASKAP (red crosses) are compared with those not detected with ASKAP (blue circles).

We suspect that sources with $|\alpha| > 3$ are the result of variability between the epochs at which the ATCA and ASKAP data were obtained. The most extreme case with $\alpha = 5.3$, EMU EC J041753.5–731556 has a spectral index of -0.69 based on SUMSS instead of ASKAP, while EMU EC J054929.5–703545 with $\alpha = 3.2$ has spectral index -1.28 when using SUMSS. The second-most extreme case, EMU EC J052029.2–680051 with $\alpha = 3.9$ sits at the edge of H II nebula LHA 120-N41 associated with emission-line star AL 139 making the comparison with ATCA data problematic. The other six radio point sources with $|\alpha| > 3$ generally have faint or no visible optical/IR counterparts in DSS, 2MASS and WISE. These could be extreme radio-variable sources at high redshift. It should be noted that at these frequencies there is the possibility of free–free absorption, which can rapidly absorb the power-law synchrotron emission spectrum towards lower radio frequencies (Clemens et al. 2010). This would cause the radio spectrum to turnover/peak, which could lead to rapid changes in spectral index, such as those seen here.

7 CONCLUSIONS

We present the 888 MHz ASKAP EMU ESP radio continuum survey of the LMC. Our findings can be summarised as follows:

- This new ASKAP survey is a significant improvement (factor of ~ 5 in the median RMS) compared to previous ATCA/MOST surveys of the LMC, and compared to the ASKAP survey of the SMC observed with a partial array (factor of ~ 3 in the median RMS). The improvement in angular resolution has also allowed for greater detail of radio structure to be observed.
- We extracted 30,866, 22,080 and 1,666 sources at 888 MHz separated into GOLD, SILVER and BRONZE source lists, respectively, with the majority of these sources detected above the 5σ threshold.
- We found 114 out of 1,334 PNe listed in Simbad to have a counterpart in ASKAP within 10 arcsec. Only 37 of these detections are likely true PNe, with the remaining sources being emission-line stars, candidate post-AGB objects, YSOs and compact H II regions.
- YSOs detected with *Herschel* (Oliveira et al. 2019) were discovered to show a strong correlation between integrated radio flux densities and gas temperature, with those with $T > 700$ K detected in radio and those with $T < 700$ K not detected in radio. This suggests a strong relation between the line emission from the photo-dissociation regions at the interfaces of neutral and ionized gas, and the free–free emission from the ionized regions surrounding the nascent, presumed massive O-type stars.
- Of 46 SNe listed in Simbad, most associated radio detections could not be unequivocally ascribed to the SN itself and are more likely emission from a background host galaxy. Only SN 1978A and Nova LMC 1988 b are securely detected with ASKAP.
- Exploring the GLEAM 4-Jy sample (White et al. 2020a,b) in the ASKAP field of the LMC revealed six GLEAM sources, showcasing that the ASKAP is an improvement in angular resolution (from $\sim 2''$ to $\leq 14''$), allowing for radio sources to be better traced to their optical/IR counterparts and revealing morphology associated with jets and likely interaction with the intra-cluster medium.
- Cross-matching the new LMC ASKAP source catalogue with AllWISE reveals 14,333 sources with photometry errors < 0.2 mag. Comparing the radio and non-radio sources reveals that the majority of the radio sources are extragalactic.

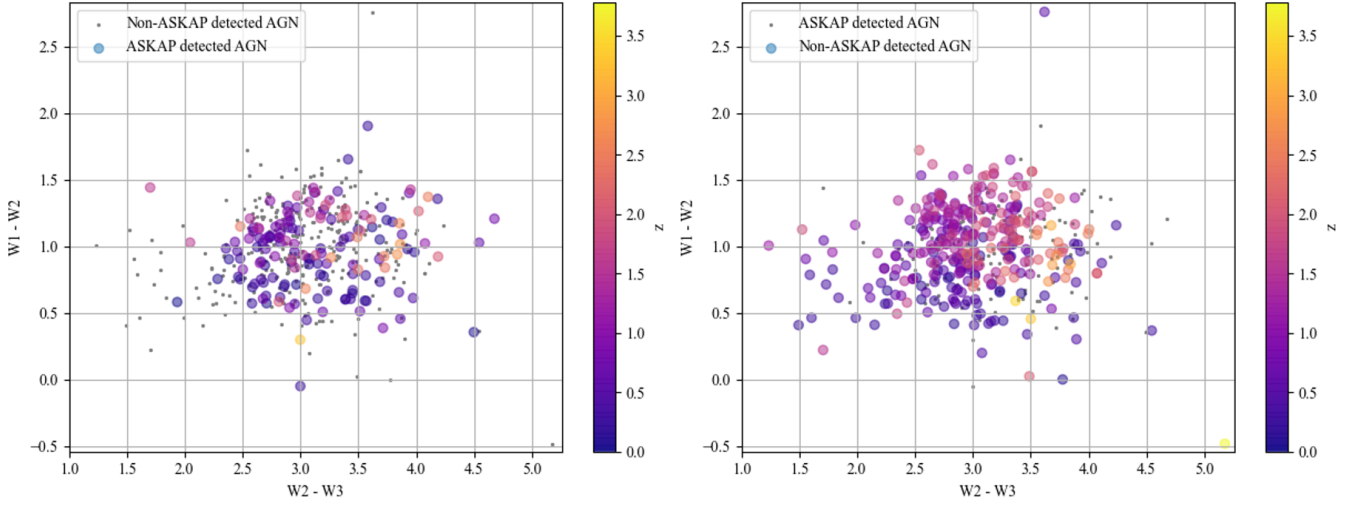


Figure 19. (Left) AllWISE colour–colour diagram of ASKAP detected AGN, where the colour indicates redshift. Grey dots indicate the non-ASKAP detected AGN. (Right) AllWISE colour–colour diagram of non-ASKAP detected AGN, where the colour indicates redshift. Grey dots indicate the ASKAP detected AGN. Both the detected and non-detected AGN show a general gradient in redshift as a function of WISE colour, with exceptions.

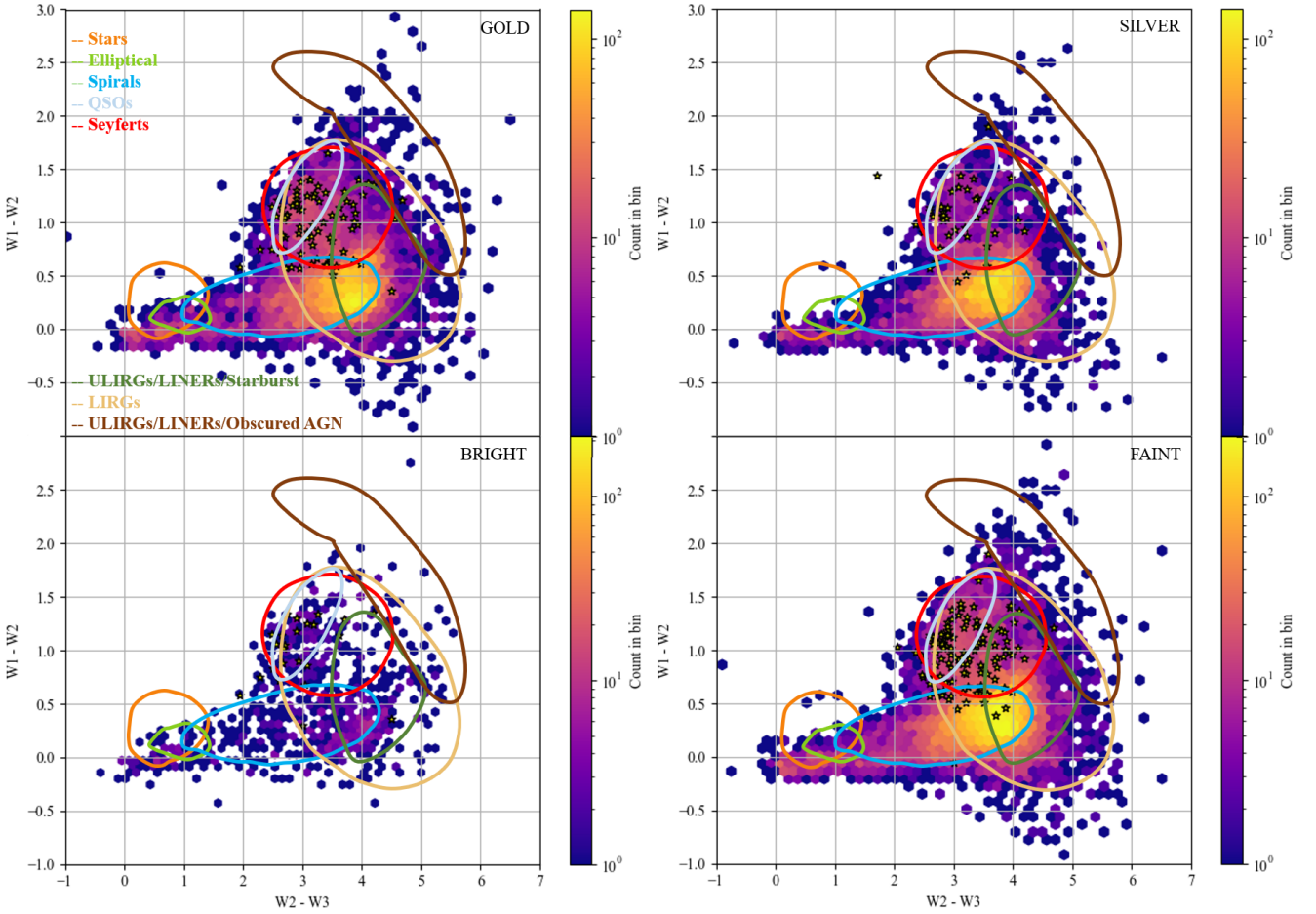


Figure 20. LMC AllWISE colour–colour diagram comparing the populations of the GOLD (top-left), SILVER (top-right), Bright (lower-left; $F_{888} > 3$ mJy) and Faint (lower-right; $F_{888} < 3$ mJy) source lists. The stars represent the spectroscopically observed AGN in their respective source list.

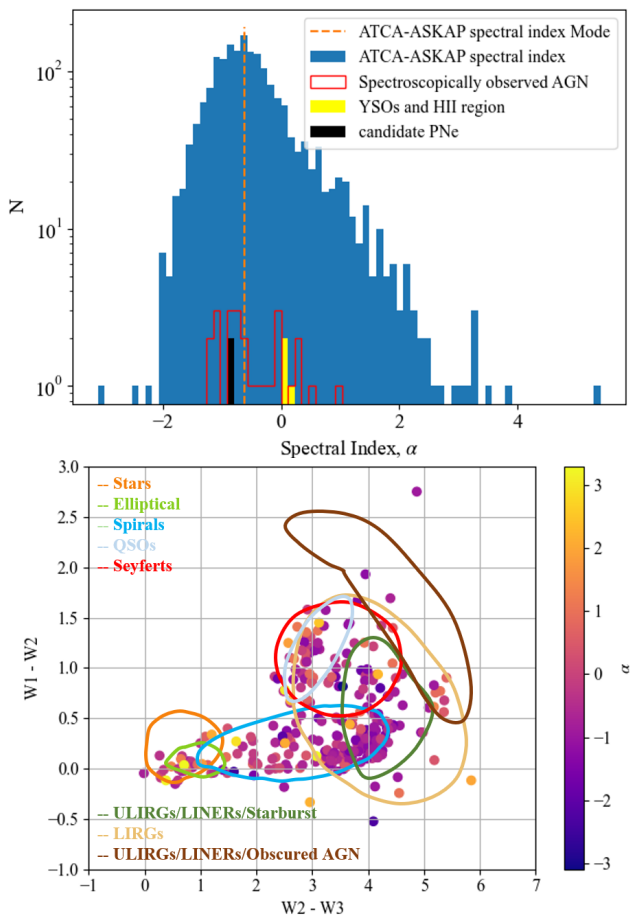


Figure 21. (Upper) Distribution of spectral indices calculated from ATCA (1.4 GHz) and ASKAP (888 MHz) integrated flux densities. (Lower) WISE colour–colour diagram of 287 sources in ASKAP, ATCA and AllWISE.

- Cross-matching the new LMC ASKAP source catalogue with the miliquas catalogue (Flesch 2019b,a) reveals 190 radio detections out of 657 spectroscopically confirmed AGN. More than 92 per cent of these are newly detected here.
- A higher fraction of AGN is found within the bright population ($F_{888} > 3$ mJy) than within the faint population ($F_{888} < 3$ mJy). As expected there is a higher fraction of spirals in the faint population compared to the bright population.
- Cross-matching the new ASKAP 888 MHz data with archival ATCA 1.4 GHz data reveals a spectral index distribution peaking at $\alpha = -0.6$ (where $F_\nu \propto \nu^\alpha$). This corroborates that the majority of sources are extragalactic synchrotron emitters. Extreme spectral indices ($|\alpha| > 3$) can be explained by variability.

Future work will include more comprehensive analyses of the planetary nebulae and supernova remnants, as well as the radio variability. We are employing machine learning to classify a combined multi-wavelength data set and study the radio–IR relation for galaxies and quasars. The background population seen in the ASKAP image shows the potential for large-scale Faraday rotation and H I absorption measurements throughout the LMC.

8 DATA AVAILABILITY

The catalogue and PNe table created in this work are available as supplementary material to this article. The image is available to the public through CASDA⁹. The catalogue, image and the PNe table will be made available on the CDS¹⁰ website when the paper is published.

ACKNOWLEDGEMENTS

We thank the anonymous referee for their feedback, which helped improve the paper. The Australian SKA Pathfinder is part of the Australia Telescope National Facility, which is managed by CSIRO. Operation of ASKAP is funded by the Australian Government with support from the National Collaborative Research Infrastructure Strategy. ASKAP uses the resources of the Pawsey Supercomputing Centre. Establishment of ASKAP, the Murchison Radio-astronomy Observatory and the Pawsey Supercomputing Centre are initiatives of the Australian Government, with support from the Government of Western Australia and the Science and Industry Endowment Fund. We acknowledge the Wajarri Yamatji people as the traditional owners of the Observatory site.

CMP is supported by an STFC studentship awarded to Keele University. M.J.M. acknowledges the support of the National Science Centre, Poland through SONATA BIS grant 2018/30/E/ST9/00208. Partial support for L.R. comes from US National Science Foundation grant AST17-14205 to the University of Minnesota. S.A. acknowledges financial support from the Centre for Research & Development in Mathematics and Applications (CIDMA) strategic project UID/MAT/04106/2019 and from Enabling Green Science for the Square Kilometre Array Research Infrastructure (ENGAGESKA), POCI-01-0145-FEDER-022217, funded by the Programa Operacional Competitividade e Internacionalização (COMPETE 2020) and FCT, Portugal. This research made use of the SIMBAD database, operated at CDS, Strasbourg, France, and the NASA/IPAC Extragalactic Database (NED) which is operated by the Jet Propulsion Laboratory, California Institute of Technology, under contract with the National Aeronautics and Space Administration.

This work has made use of Python software packages: *aegean*¹¹, *astropy*¹², *numpy*¹³, *pandas*¹⁴ and *matplotlib*¹⁵.

REFERENCES

- Abbott T. M. C., et al., 2018, *ApJS*, **239**, 18
 Agliozzo C., Umata G., Trigilio C., Buemi C., Leto P., Ingallinera A., Franzen T., Noriega-Crespo A., 2012, *MNRAS*, **426**, 181
 Agliozzo C., et al., 2017a, *MNRAS*, **466**, 213
 Agliozzo C., et al., 2017b, *ApJ*, **841**, 130
 Agliozzo C., et al., 2019, *A&A*, **626**, A126
 Akra S., Guzman-Ramirez L., Leal-Ferreira M. L., Ramos-Larios G., 2019, *ApJS*, **240**, 21
 Antoniou V., Zezas A., 2016, *MNRAS*, **459**, 528

⁹ <https://research.csiro.au/casda/>

¹⁰ <https://cds.u-strasbg.fr/>

¹¹ <https://github.com/PaulHancock/Aegean>

¹² <http://www.astropy.org>

¹³ <http://numpy.org>

¹⁴ <http://pandas.pydata.org>

¹⁵ <http://matplotlib.org>

- Assef R. J., et al., 2013, *ApJ*, **772**, 26
- Azulay R., et al., 2015, *A&A*, **578**, A16
- Azulay R., et al., 2017, *A&A*, **607**, A10
- Baars J. W. M., Genzel R., Pauliny-Toth I. I. K., Witzel A., 1977, *A&A*, **500**, 135
- Bailer-Jones C. A. L., Fouesneau M., Andrae R., 2019, *MNRAS*, **490**, 5615
- Barenfeld S. A., Bubar E. J., Mamajek E. E., Young P. A., 2013, *ApJ*, **766**, 6
- Beasley A. J., Cram L. E., 1993, *MNRAS*, **264**, 570
- Bianchi L., Pakull M., 1984, in Mead J. M., Chapman R. D., Kondo Y., eds, NASA Conference Publication Vol. 2349, NASA Conference Publication. pp 416–419
- Bilicki M., Jarrett T. H., Peacock J. A., Cluver M. E., Steward L., 2014, *ApJS*, **210**, 9
- Bilicki M., et al., 2016, *ApJS*, **225**, 5
- Burgess A. M., Hunstead R. W., 2006, *AJ*, **131**, 114
- Callingham J. R., et al., 2016, *MNRAS*, **462**, 290
- Chen C. H. R., Chu Y.-H., Gruendl R. A., Gordon K. D., Heitsch F., 2009, *ApJ*, **695**, 511
- Cioni M. R. L., et al., 2011, *A&A*, **527**, A116
- Cioni M. R. L., et al., 2017, VizieR Online Data Catalog, p. II/351
- Clemens M. S., Scaife A., Vega O., Bressan A., 2010, *MNRAS*, **405**, 887
- Climent J. B., Berger J. P., Guirado J. C., Marcaide J. M., Martí-Vidal I., Mérand A., Tognelli E., Wittkowski M., 2019, *AJ*, **886**, L9
- Collier A. C., 1982, *MNRAS*, **200**, 489
- Collier Cameron A., Bedford D. K., Rucinski S. M., Vilhu O., White N. E., 1988, *MNRAS*, **231**, 131
- Costa E., Méndez R. A., Pedreros M. H., Moyano M., Gallart C., Noël N., Baume G., Carraro G., 2009, *AJ*, **137**, 4339
- Cowley A. P., Crampton D., Hutchings J. B., Helfand D. J., Hamilton T. T., Thorstensen J. R., Charles P. A., 1984, *ApJ*, **286**, 196
- Coziol R., Andernach H., Caretta C. A., Alamo-Martínez K. A., Tago E., 2009, *AJ*, **137**, 4795
- Cutri R. M., et al., 2013, Explanatory Supplement to the AllWISE Data Release Products, Explanatory Supplement to the AllWISE Data Release Products
- Dállya G., et al., 2018, *MNRAS*, **479**, 2374
- DeBoer D. R., et al., 2009, *IEEE Proceedings*, **97**, 1507
- Dickel J. R., McIntyre V. J., Gruendl R. A., Milne D. K., 2005, *AJ*, **129**, 790
- Dickey J. M., et al., 2013, *Publ. Astron. Soc. Australia*, **30**, e003
- Donati J. F., Collier Cameron A., 1997, *MNRAS*, **291**, 1
- Donati J. F., Collier Cameron A., Hussain G. A. J., Semel M., 1999, *MNRAS*, **302**, 437
- Esquej P., et al., 2013, *A&A*, **557**, A123
- Fanaroff B. L., Riley J. M., 1974, *MNRAS*, **167**, 31P
- Filipović M. D., et al., 2021, *MNRAS*, submitted
- Filipovic M. D., Haynes R. F., White G. L., Jones P. A., Klein U., Wielebinski R., 1995, *A&AS*, **111**, 311
- Filipovic M. D., White G. L., Haynes R. F., Jones P. A., Meinert D., Wielebinski R., Klein U., 1996, *A&AS*, **120**, 77
- Filipovic M. D., Jones P. A., White G. L., Haynes R. F., 1998a, *Publ. Astron. Soc. Australia*, **15**, 128
- Filipovic M. D., et al., 1998b, *A&AS*, **127**, 119
- Filipovic M. D., Haynes R. F., White G. L., Jones P. A., 1998c, *A&AS*, **130**, 421
- Filipovic M. D., Haynes R. F., White G. L., Jones P. A., 1998d, *A&AS*, **130**, 421
- Filipovic M. D., Jones P. A., White G. L., Haynes R. F., 1998e, *A&AS*, **130**, 441
- Filipović M. D., et al., 2009, *MNRAS*, **399**, 769
- Flesch E. W., 2015, *Publ. Astron. Soc. Australia*, **32**, e010
- Flesch E. W., 2019a, VizieR Online Data Catalog, p. VII/283
- Flesch E. W., 2019b, arXiv e-prints, p. arXiv:1912.05614
- For B. Q., et al., 2018, *MNRAS*, **480**, 2743
- Fuhrmeister B., Schmitt J. H. M. M., 2003, *Astronomische Nachrichten Supplement*, **324**, 32
- Gaia Collaboration et al., 2018a, *A&A*, **616**, A1
- Gaia Collaboration et al., 2018b, *A&A*, **616**, A1
- Geha M., et al., 2003, *AJ*, **125**, 1
- Grazian A., Omizzolo A., Corbally C., Cristiani S., Haehnelt M. G., Vanzella E., 2002, *AJ*, **124**, 2955
- Griffith M. R., Wright A. E., 1993, *AJ*, **105**, 1666
- Güdel M., 2002, *ARA&A*, **40**, 217
- Haberl F., 2014, in Ness J.-U., ed., *The X-ray Universe 2014*. p. 4
- Haberl F., Pietsch W., 1999a, *A&AS*, **139**, 277
- Haberl F., Pietsch W., 1999b, *A&A*, **344**, 521
- Haberl F., Sturm R., 2016, *A&A*, **586**, A81
- Haberl F., Dennerl K., Filipović M. D., Aschenbach B., Pietsch W., Trümper J., 2001, *A&A*, **365**, L208
- Hale C. L., Robotham A. S. G., Davies L. J. M., Jarvis M. J., Driver S. P., Heywood I., 2019, *MNRAS*, **487**, 3971
- Hancock P. J., Murphy T., Gaensler B. M., Hopkins A., Curran J. R., 2012, *MNRAS*, **422**, 1812
- Hancock P. J., Trott C. M., Hurley-Walker N., 2018, *Publ. Astron. Soc. Australia*, **35**, e011
- Heydari-Malayeri M., Melnick J., 1992, *A&A*, **258**, L13
- Hotan A. W., et al., 2014, *Publ. Astron. Soc. Australia*, **31**, e041
- Hotan A. W., et al., 2021, *Publ. Astron. Soc. Australia*, **38**, e009
- Huchra J. P., et al., 2012, *ApJS*, **199**, 26
- Hughes A., Staveley-Smith L., Kim S., Wolleben M., Filipović M., 2007, *MNRAS*, **382**, 543
- Hyde E. A., Russell D. M., Ritter A., Filipović M. D., Kaper L., Grieve K., O'Brien A. N., 2017, *PASP*, **129**, 094201
- Innis J. L., Thompson K., Coates D. W., 1986, *MNRAS*, **223**, 183
- Ivanov V. D., et al., 2016, *A&A*, **588**, A93
- Jardine M., Collier Cameron A., Donati J. F., 2002, *MNRAS*, **333**, 339
- Jarrett T. H., et al., 2011, *ApJ*, **735**, 112
- Johnston S., et al., 2008, *Experimental Astronomy*, **22**, 151
- Jones D. H., et al., 2009, *MNRAS*, **399**, 683
- Joseph T. D., et al., 2019, *MNRAS*, **490**, 1202
- Joye W. A., Mandel E., 2003, in Payne H. E., Jędrzejewski R. I., Hook R. N., eds, *Astronomical Society of the Pacific Conference Series Vol. 295, Astronomical Data Analysis Software and Systems XII*. p. 489
- Kahabka P., 2002, *A&A*, **388**, 100
- Kallivayalil N., van der Marel R. P., Alcock C., Axelrod T., Cook K. H., Drake A. J., Geha M., 2006, *ApJ*, **638**, 772
- Kim S., Staveley-Smith L., Dopita M. A., Freeman K. C., Sault R. J., Kesteven M. J., McConnell D., 1998, *ApJ*, **503**, 674
- Kim S., Staveley-Smith L., Dopita M. A., Sault R. J., Freeman K. C., Lee Y., Chu Y.-H., 2003, *ApJS*, **148**, 473
- Kozłowski S., et al., 2012, *ApJ*, **746**, 27
- Kozłowski S., et al., 2013, *ApJ*, **775**, 92
- Krogager J. K., et al., 2018, *ApJS*, **235**, 10
- Lakićević M., van Loon J. T., Patat F., Staveley-Smith L., Zanardo G., 2011, *A&A*, **532**, L8
- Large M. I., Mills B. Y., Little A. G., Crawford D. F., Sutton J. M., 1981, *MNRAS*, **194**, 693
- Leahy D. A., et al., 2019, *Publ. Astron. Soc. Australia*, **36**, e024
- Leavitt H. S., 1908, *Annals of Harvard College Observatory*, **60**, 87
- Leavitt H. S., Pickering E. C., 1912, *Harvard College Observatory Circular*, **173**, 1
- Leverenz H., Filipović M. D., Vukotić B., Urošević D., Grieve K., 2017, *MNRAS*, **468**, 1794
- Lim J., 1993, *ApJ*, **405**, L33
- Marocco F., et al., 2021, *ApJS*, **253**, 8
- Mateos S., et al., 2012, *MNRAS*, **426**, 3271
- Mathewson D. S., Cleary M. N., Murray J. D., 1974, *ApJ*, **190**, 291
- Mauch T., Murphy T., Buttery H. J., Curran J., Hunstead R. W., Piestrzynski B., Robertson J. G., Sadler E. M., 2003a, VizieR Online Data Catalog, p. VIII/70A
- Mauch T., Murphy T., Buttery H. J., Curran J., Hunstead R. W., Piestrzynski B., Robertson J. G., Sadler E. M., 2003b, *MNRAS*, **342**, 1117
- McConnell D., Sadler E. M., Murphy T., Ekers R. D., 2012, *MNRAS*, **422**, 1527
- McConnell D., et al., 2016, *Publ. Astron. Soc. Australia*, **33**, e042
- McConnell D., et al., 2020, *Publ. Astron. Soc. Australia*, **37**, e048
- Mehner A., et al., 2017, *A&A*, **608**, A124

- Meixner M., et al., 2006, *AJ*, **132**, 2268
- Meixner M., et al., 2010, *A&A*, **518**, L71
- Mills B. Y., 1985, *Proceedings of the Astronomical Society of Australia*, **6**, 72
- Morgan D. H., Watson F. G., Parker Q. A., 1992, *A&AS*, **93**, 495
- Morris D. H., Mutel R. L., 1988, *AJ*, **95**, 204
- Murai T., Fujimoto M., 1980, *PASJ*, **32**, 581
- Murphy T., et al., 2010, *MNRAS*, **402**, 2403
- Murphy T., et al., 2013, *Publ. Astron. Soc. Australia*, **30**, e006
- Negueruela I., Coe M. J., 2002, *A&A*, **385**, 517
- Ng C. Y., Zanardo G., Potter T. M., Staveley-Smith L., Gaensler B. M., Manchester R. N., Tzioumis A. K., 2013, *ApJ*, **777**, 131
- Nidever D. L., et al., 2017, *AJ*, **154**, 199
- Nikutta R., Hunt-Walker N., Nenkova M., Ivezić v., Elitzur M., 2014, *MNRAS*, **442**, 3361
- Oliveira J. M., Foing B. H., 1999, *A&A*, **343**, 213
- Oliveira J. M., et al., 2019, *MNRAS*, **490**, 3909
- Ortega V. G., Jilinski E., de La Reza R., Bazzanella B., 2007, *MNRAS*, **377**, 441
- Pakull M. W., 1981, *A&A*, **104**, 33
- Pedrerros M. H., 2011, *Rev. Mex. Astron. Astrofis.*, **47**, 333
- Pietrzyński G., et al., 2013, *Nature*, **495**, 76
- Pietrzyński G., et al., 2019, *Nature*, **567**, 200
- Riess A. G., Casertano S., Yuan W., Macri L. M., Scolnic D., 2019, *ApJ*, **876**, 85
- Riggi S., et al., 2021, *MNRAS*, **502**, 60
- Rucinski S. M., 1983, *A&AS*, **52**, 281
- Sanz-Forcada J., Maggio A., Micela G., 2003, *A&A*, **408**, 1087
- Saulder C., van Kampen E., Chilingarian I. V., Mieske S., Zeilinger W. W., 2016, *A&A*, **596**, A14
- Schmidt T., et al., 2020, *A&A*, **641**, A134
- Schmidtke P. C., Cowley A. P., Crane J. D., Taylor V. A., McGrath T. K., Hutchings J. B., Crampton D., 1999, *AJ*, **117**, 927
- Sekiguchi K., Kilkenny D., Winkler H., Doyle J. G., 1989, *MNRAS*, **241**, 827
- Sewilo M., et al., 2018, *AJ*, **853**, L19
- Shafter A. W., 2013, *AJ*, **145**, 117
- Shtykovskiy P., Gilfanov M., 2005, *A&A*, **431**, 597
- Skowron D. M., et al., 2020, arXiv e-prints, p. arXiv:2006.02448
- Slee O. B., Haynes R. F., Wright A. E., 1984, *MNRAS*, **208**, 865
- Slee O. B., Nelson G. J., Stewart R. T., Wright A. E., Innis J. L., Ryan S. G., Vaughan A. E., 1987, *MNRAS*, **229**, 659
- Stern D., et al., 2012, *ApJ*, **753**, 30
- Subrahmanyan R., Saripalli L., Hunstead R. W., 1996, *MNRAS*, **279**, 257
- Szczygieł D. M., Socrates A., Paczyński B., Pojmański G., Pilecki B., 2008, *Acta Astron.*, **58**, 405
- Taylor M. B., 2005, in Shopbell P., Britton M., Ebert R., eds, *Astronomical Society of the Pacific Conference Series Vol. 347, Astronomical Data Analysis Software and Systems XIV* p. 29
- Torres C. A. O., Quast G. R., da Silva L., de La Reza R., Melo C. H. F., Sterzik M., 2006, *A&A*, **460**, 695
- Vaughan A. E., Large M. I., 1986, *Proceedings of the Astronomical Society of Australia*, **6**, 319
- Vaughan A. E., Large M. I., 1987, *Proceedings of the Astronomical Society of Australia*, **7**, 42
- Vieira K., et al., 2014, in *Revista Mexicana de Astronomía y Astrofísica Conference Series*. pp 51–54
- Webb N. A., et al., 2020, *A&A*, **641**, A136
- Wegner G., et al., 2003, *AJ*, **126**, 2268
- Weis K., 2003, *A&A*, **408**, 205
- Wendker H. J., 1995, *A&AS*, **109**, 177
- White G. L., Jauncey D. L., Batty M. J., Peters W. L., Gulkis S., 1988, *PASP*, **100**, 825
- White S. V., et al., 2020a, *Publ. Astron. Soc. Australia*, **37**, e017
- White S. V., et al., 2020b, *Publ. Astron. Soc. Australia*, **37**, e018
- Whiting M. T., 2020, in Ballester P., Ibsen J., Solar M., Shortridge K., eds, *Astronomical Society of the Pacific Conference Series Vol. 522, Astronomical Data Analysis Software and Systems XXVII* p. 469
- Wolf C., et al., 2018, *Publ. Astron. Soc. Australia*, **35**, e010
- Wolter U., Czesla S., Fuhrmeister B., Robrade J., Engels D., Wieringa M., Schmitt J. H. M. M., 2014, *A&A*, **570**, A95
- Wright E. L., et al., 2010, *AJ*, **140**, 1868
- van Aarle E., van Winckel H., Lloyd Evans T., Ueta T., Wood P. R., Ginsburg A. G., 2011, *A&A*, **530**, A90
- van Loon J. T., Zijlstra A. A., Bujarrabal V., Nyman L. Å., 2001, *A&A*, **368**, 950
- van Loon J. T., Cioni M. R. L., Zijlstra A. A., Loup C., 2005, *A&A*, **438**, 273
- van Loon J. T., et al., 2010, *AJ*, **139**, 68
- van der Marel R. P., Kallivayalil N., 2014, *ApJ*, **781**, 121
- ²Western Sydney University, Locked Bag 1797, Penrith South DC, NSW 2751, Australia
- ³Depto. de Astronomía, DCNE, Universidad de Guanajuato, Cjón. de Jalisco s/n, Col. Valenciana, Guanajuato, CP 36023, Gto., México
- ⁴Max-Planck-Institut für extraterrestrische Physik, Gießenbachstraße 1, D-85748 Garching bei München, Germany
- ⁵Dominion Radio Astrophysical Observatory, Herzberg Programs in Astronomy and Astrophysics, National Research Council Canada, P.O. Box 248, Penticton, BC V2A 6J9, Canada
- ⁶Australia Telescope National Facility, CSIRO Astronomy and Space Science, P.O. Box 76, Epping, NSW 1710, Australia
- ⁷Minnesota Institute for Astrophysics, School of Physics and Astronomy, University of Minnesota, 116 Church Street SE, Minneapolis, MN 55455, USA
- ⁸Department of Physics and Electronics, Rhodes University, P.O. Box 94, Grahamstown, 6140, South Africa
- ⁹European Southern Observatory, Karl-Schwarzschild-Strasse 2, Garching bei München, 85748, Germany
- ¹⁰Centre for Research and Development in Mathematics and Applications (CIDMA), Campus de Santiago, 3810-183 Aveiro, Portugal
- ¹¹Research Department, Plasmas with Complex Interactions, Ruhr-Universität Bochum, 44780 Bochum, Germany
- ¹²Astronomisches Institut, Ruhr-Universität Bochum, 44780 Bochum, Germany
- ¹³The Inter-University Institute for Data Intensive Astronomy (IDIA), Department of Astronomy, University of Cape Town, Rondebosch 7701, South Africa
- ¹⁴Australian Astronomical Optics, Macquarie University, 105 Delhi Rd., North Ryde, NSW 2113, Australia
- ¹⁵CSIRO Astronomy and Space Science, Radiophysics Laboratory, Marsfield, NSW, Australia
- ¹⁶School of Cosmic Physics, Dublin Institute for Advanced Studies, 31 Fitzwilliam Place, Dublin 2, Ireland
- ¹⁷Department of Physics and Astronomy, University of Calgary, University of Calgary, Calgary, Alberta, T2N 1N4, Canada
- ¹⁸Observatoire Astronomique de Strasbourg, Université de Strasbourg, CNRS, 11 rue de l'Université, F-67000 Strasbourg, France
- ¹⁹National Radio Astronomy Observatory, 1003 Lopezville Rd., Socorro, NM 87801, USA
- ²⁰Astronomical Observatory Institute, Faculty of Physics, Adam Mickiewicz University, ul. Słoneczna 36, 60-286 Poznań, Poland
- ²¹National Astronomical Observatory of Japan, Mitaka, Tokyo 181-8588, Japan
- ²²Department of Physics, Nagoya University, Furo-cho, Chikusa-ku, Nagoya 464-8601, Japan
- ²³Institute for Advanced Research, Nagoya University, Furo-cho,

Chikusa-ku, Nagoya 464-8601, Japan

²⁴*Remeis Observatory and ECAP, Universität Erlangen-Nürnberg,
Sternwartstraße 7, D-96049 Bamberg, Germany*

²⁵*International Centre for Radio Astronomy Research, University
of Western Australia, 35 Stirling Hwy, Crawley, WA 6009, Australia*

²⁶*ARC Centre of Excellence for All Sky Astrophysics in 3 Dimen-
sions (ASTRO 3D)*

²⁷*Thüringer Landessternwarte, Sternwarte 5, 07778 Tautenburg,
Germany*

This paper has been typeset from a $\text{\TeX}/\text{\LaTeX}$ file prepared by the author.